REPORT DOCUMENTATION PAGE

Form Approved OMB NO. 0704-0188

1. REPORT DATE (DD-MM-YYYY)	2. REPORT TYPE	3. DATES COVERED (From - To)
27-01-2012	Final Report	1-Jun-2006 - 30-Nov-2010

4. TITLE AND SUBTITLE	5a. CONTRACT NUMBER
Final Report on Photonic Devices Based on Surface and Composition-Engineered Infrared Colloidal Nanocrystals (ARO Proposal No: 49653-EL)	W911NF-06-1-0211
	5b. GRANT NUMBER
	5c. PROGRAM ELEMENT NUMBER
	611102

6. AUTHORS	5d. PROJECT NUMBER
Jian Xu	
	5e. TASK NUMBER
	5f. WORK UNIT NUMBER

7. PERFORMING ORGANIZATION NAMES AND ADDRESSES	8. PERFORMING ORGANIZATION REPORT NUMBER
Pennsylvania State University Office of Sponsored Programs The Pennsylvania State University University Park, PA 16802 -7000	

9. SPONSORING/MONITORING AGENCY NAME(S) AND ADDRESS(ES)	10. SPONSOR/MONITOR'S ACRONYM(S) ARO
U.S. Army Research Office P.O. Box 12211 Research Triangle Park, NC 27709-2211	11. SPONSOR/MONITOR'S REPORT NUMBER(S) 49653-EL.41

12. DISTRIBUTION AVAILIBILITY STATEMENT

Approved for Public Release; Distribution Unlimited

13. SUPPLEMENTARY NOTES

14. ABSTRACT

Abstract
The goal of this ARO sponsored project is to develop advanced photonic devices based on surface and composition engineered semiconductor nanocrystals. The PI's laboratory has successfully carried out and exceeded the proposed goals of the project with a series of scientific findings and promising technical results. These achievements can be categorized into two major groups. The first group consists of advances in semiconductor

15. SUBJECT TERMS

semiconductor nanocrystals, quantum dots, nanoparticles, photovoltaic devices, solar cells, luminescent solar concentrators, light emitting diodes, lasers, photonic crystals, CdSe, PbSe, Germanium

16. SECURITY CLASSIFICATION OF:			17. LIMITATION OF ABSTRACT	15. NUMBER OF PAGES	19a. NAME OF RESPONSIBLE PERSON
a. REPORT	b. ABSTRACT	c. THIS PAGE	UU		Jian Xu
UU	UU	UU			19b. TELEPHONE NUMBER 814-863-0721

Final Report on Photonic Devices Based on Surface and Composition-Engineered Infrared Colloidal Nanocrystals (ARO Proposal No: 49653-EL)

ABSTRACT

Abstract

The goal of this ARO sponsored project is to develop advanced photonic devices based on surface and composition engineered semiconductor nanocrystals. The PI's laboratory has successfully carried out and exceeded the proposed goals of the project with a series of scientific findings and promising technical results. These achievements can be categorized into two major groups. The first group consists of advances in semiconductor nanocrystal-based photovoltaic technology, including thin film solar cells, luminescent solar concentrators, and photonic absorbers, while the second group is composed of accomplishments in nanocrystal light-emitting-diodes (LEDs), nanolasers, and germanium emitters. Among these achievements are the first demonstration of PbSe nanocrystal photovoltaic devices and planar-mixed heterojunction quantum dot solar cells, the first observation of two-photon absorption induced lasing in semiconductor nanocrystals, the design and fabrication of the first photonic crystal-enhanced nanocrystals infrared LED, the first Monte Carlo simulation of infrared luminescent solar concentrator using nanocrystals fluorophores, and the first demonstration of efficient near-band-edge electroluminescence emission from heavy-metal-free semiconductor nanoparticles. These findings and technical results open up new avenues to develop high-performance, environmentally-friend and mass-producible photonic devices with state-of-the-art colloidal semiconductor technology.

Enter List of papers submitted or published that acknowledge ARO support from the start of the project to the date of this printing. List the papers, including journal references, in the following categories:

(a) Papers published in peer-reviewed journals (N/A for none)

Received	Paper
2012/01/24 1: 28	Z. Wu, Z. Mi, P. Bhattacharya, T. Zhu, J. Xu. Enhanced spontaneous emission at 1.55??m from colloidal PbSe quantum dots in a Si photonic crystal microcavity, Applied Physics Letters, (04 2007): 0. doi: 10.1063/1.2731657
2012/01/24 1: 22	S C Price, K Shanmugasundaram, S Ramani, T Zhu, F Zhang, J Xu, S E Mohney, Q Zhang, A Kshirsagar, J Ruzyllo. Studies of mist deposition for the formation of quantum dot CdSe films, Semiconductor Science and Technology, (10 2009): 0. doi: 10.1088/0268-1242/24/10/105024
2012/01/23 1: 40	Li Chen, Hongjun Yang, Zexuan Qiang, Huiqing Pang, Lei Sun, Zhenqiang Ma, Ryan Pate, Adrienne Stiff-Roberts, Shuai Gao, Jian Xu, Gail J. Brown, Weidong Zhou. Colloidal quantum dot absorption enhancement in flexible Fano filters, Applied Physics Letters, (02 2010): 0. doi:
2012/01/23 1: 33	Chunfeng Zhang, Fan Zhang, Tian Xia, Nitin Kumar, Jong-in Hahm, Jin Liu, Zhong Lin Wang, Jian Xu. Low-threshold two-photon pumped ZnO nanowire lasers, Optics Express, (04 2009): 0. doi: 10.1364/OE.17.007893
2012/01/23 1(32	Shuai Gao, Chunfeng Zhang, Yanjun Liu, Huaipeng Su, Lai Wei, Tony Huang, Nicholas Dellas, Shuzhen Shang, Suzanne E. Mohney, Jingkang Wang, Jian Xu. Lasing from colloidal InP/ZnS quantum dots, Optics Express, (03 2011): 0. doi: 10.1364/OE.19.005528
2012/01/23 1(31	Junseok Heo, Zhenyu Jiang, Jian Xu, Pallab Bhattacharya. Coherent and directional emission at 155 ?m from PbSe colloidal quantum dot electroluminescent device on silicon, Optics Express, (12 2011): 0. doi: 10.1364/OE.19.026394
2012/01/23 1(30	J XU, A LAKHTAKIA, J LIOU, A CHEN, I HODGKINSON. Circularly polarized fluorescence from light-emitting microcavities with sculptured-thin-film chiral reflectors, Optics Communications, (08 2006): 0. doi: 10.1016/j.optcom.2006.02.025
2012/01/23 1(29	Qing Wang, Jian Xu, Dehu Cui, Ting Zhu, Gary Paradee, Ziqi Liang, Andrew Y Wang, Shengyong Xu. Synthesis and surface modification of PbSe/PbS core–shell nanocrystals for potential device applications, Nanotechnology, (11 2006): 0. doi: 10.1088/0957-4484/17/21/024
2012/01/23 1(27	Wanming Zhang, Jian Xu, Hongying Peng, Henry O. Everitt, Adrienne D. Stiff-Roberts. Spin-Cast Deposition of CdSe-CdS Core-Shell Colloidal Quantum Dots on Doped GaAs Substrates: Structural and Optical Characterization, IEEE Transactions on Nanotechnology, (07 2007): 0. doi: 10.1109/TNANO.2007.896845
2012/01/23 1(25	Jian Xu, Chunhe Yang, Yongfang Li, Ting Zhu, Qingjiang Sun, Y. Andrew Wang, Lin Song Li, Daoyuan Wang. Bright, multicoloured light-emitting diodes based on quantum dots, Nature Photonics, (11 2007): 0. doi: 10.1038/nphoton.2007.226
2012/01/23 1(24	Dehu Cui, Jian Xu, Gary Paradee, Shengyong Xu, Andrew Y. Wang. Developing PbSe/PbS core-shell nanocrystals quantum dots toward their potential heterojunction applications, Journal of Experimental Nanoscience, (03 2007): 0. doi: 10.1080/17458080600935590
2012/01/23 1(23	Jian Xu, Chunfeng Zhang, Fan Zhang, Shixiong Qian, Nitin Kumar, Jong-in Hahm. Multiphoton absorption induced amplified spontaneous emission from biocatalyst-synthesized ZnO nanorods, Applied Physics Letters, (06 2008): 0. doi: 10.1063/1.2927486
2012/01/23 0! 20	Zhanao Tan, Ting Zhu, Myo Thein, Shuai Gao, An Cheng, Fan Zhang, Chunfeng Zhang, Huaipeng Su, Jingkang Wang, Ron Henderson, Jong-in Hahm, Yongping Yang, Jian Xu. Integration of planar and bulk heterojunctions in polymer/nanocrystal hybrid photovoltaic cells, Applied Physics Letters, (08 2009): 0. doi: 10.1063/1.3189083
2012/01/23 0! 16	Zhanao Tan, Yu Zhang, Chuang Xie, Huaipeng Su, Jie Liu, Chunfeng Zhang, Nicholas Dellas, Suzanne E. Mohney, Yongqiang Wang, Jingkang Wang, Jian Xu. Near-Band-Edge Electroluminescence from Heavy-Metal-Free Colloidal Quantum Dots, Advanced Materials, (08 2011): 0. doi: 10.1002/adma.201100719
2012/01/23 0! 5	Jun Yang, Junseok Heo, Ting Zhu, Jian Xu, Juraj Topolancik, Frank Vollmer, Rob Ilic, Pallab Bhattacharya. Enhanced photoluminescence from embedded PbSe colloidal quantum dots in silicon-based random photonic crystal microcavities, Applied Physics Letters, (07 2008): 0. doi: 10.1063/1.2954007

2012/01/23 0! 12   Zhanao Tan, B. Hedrick, Fan Zhang, Ting Zhu, Jian Xu, R.H. Henderson, J. Ruzyllo, A.Y. Wang. Stable Binary Complementary White Light-Emitting Diodes Based on Quantum-Dot/Polymer-Bilayer Structures, IEEE Photonics Technology Letters, (12 2008): 0. doi: 10.1109/LPT.2008.2006278

2012/01/23 0! 11   Chunfeng Zhang, Fan Zhang, Ting Zhu, An Cheng, Jian Xu, Qi Zhang, Suzanne E. Mohney, Ron H. Henderson, Y. Andrew Wang. Two-photon-pumped lasing from colloidal nanocrystal quantum dots, Optics Letters, (11 2008): 0. doi: 10.1364/OL.33.002437

2012/01/23 0! 8   Chunfeng Zhang, Fan Zhang, Xiao Wei Sun, Yi Yang, Jian Wang, Jian Xu. Frequency-upconverted whispering-gallery-mode lasing in ZnO hexagonal nanodisks, Optics Letters, (11 2009): 0. doi: 10.1364/OL.34.003349

2012/01/23 0! 14   Junseok Heo, Ting Zhu, Chunfeng Zhang, Jian Xu, Pallab Bhattacharya. Electroluminescence from silicon-based photonic crystal microcavities with PbSe quantum dots, Optics Letters, (02 2010): 0. doi: 10.1364/OL.35.000547

2012/01/23 0! 9   Chunfeng Zhang, Jian Xu, Ting Zhu, Fan Zhang, Zhanao Tan, Steven Schiff, Huaipeng Su, Shuai Gao, Andrew Wang. Quantum efficiency of stimulated emission in colloidal semiconductor nanocrystal quantum dots, Physical Review B, (07 2009): 0. doi: 10.1103/PhysRevB.80.035333

2012/01/23 0! 4   T. Zhu, K. Shanmugasundaram, S. C. Price, J. Ruzyllo, F. Zhang, J. Xu, S. E. Mohney, Q. Zhang, A. Y. Wang. Mist fabrication of light emitting diodes with colloidal nanocrystal quantum dots, Applied Physics Letters, (01 2008): 0. doi: 10.1063/1.2834734

2012/01/23 0! 15   Jian Xu, Akhlesh Lakhtakia, Sean M. Pursel, Mark W. Horn, Andrew Wang, Fan Zhang. Circularly polarized emission from colloidal nanocrystal quantum dots confined in microcavities formed by chiral mirrors, Applied Physics Letters, (07 2007): 0. doi: 10.1063/1.2751129

2012/01/23 0! 10   Jian Xu, Chunfeng Zhang, Ting Zhu, Fan Zhang, Brittany Hedrick, Shawn Pickering, Jian Wu, Huaipeng Su, Shuai Gao, Andrew Y. Wang, Zhanao Tan, Brian Kimball, Jerzy Ruzyllo, Nicholas S. Dellas, Suzanne E. Mohney. Colloidal nanocrystal-based light-emitting diodes fabricated on plastic toward flexible quantum dot optoelectronics, Journal of Applied Physics, (02 2009): 0. doi: 10.1063/1.3074335

2012/01/23 0! 6   Zhanao Tan, Fan Zhang, Ting Zhu, Jian Xu, Andrew Y. Wang, John D. Dixon, Linsong Li, Qi Zhang, Suzanne E. Mohney, Jerzy Ruzyllo. Bright and Color-Saturated Emission from Blue Light-Emitting Diodes Based on Solution-Processed Colloidal Nanocrystal Quantum Dots, Nano Letters, (12 2007): 0. doi: 10.1021/nl072370s

2012/01/21 1! 2   Fan Zhang, Chunfeng Zhang, Andrew Y. Wang, Jian Xu. Frequency upconverted lasing of nanocrystal quantum dots in microbeads, Applied Physics Letters, (01 2009): 0. doi: 10.1063/1.3242352

    TOTAL: **25**

Number of Papers published in peer-reviewed journals:

(b) Papers published in non-peer-reviewed journals (N/A for none)

<u>Received</u>   <u>Paper</u>

    TOTAL:

Number of Papers published in non peer-reviewed journals:

(c) Presentations

1. J. Xu, "Bright and Color-Saturated Light Emitting Devices Based on Colloidal Nanocrystal Quantum Dots", AVS 54 International Symposium, Seattle, Washington, October 15-19, 2007 (Invited speaker)
2. J ian Xu"Colloidal Nanocrystal-Based LEDs and LED Matrix Arrays Fabricated on Plastic" Workshop on the Research Frontiers of Solid State Lighting, NTU Singapore, November 2009
3. Jian Xu "Nonradiative energy transfer to colloidal nanocrystal quantum dots" (Invited Paper) SPIE Photonics West, San Francisco, January 2010

Number of Presentations: 3.00

Non Peer-Reviewed Conference Proceeding publications (other than abstracts):

<u>Received</u>   <u>Paper</u>

   TOTAL:

Number of Non Peer-Reviewed Conference Proceeding publications (other than abstracts):

Peer-Reviewed Conference Proceeding publications (other than abstracts):

<u>Received</u>   <u>Paper</u>

2012/01/24 1: 18   Li Chen, Hongjun Yang, Zexuan Qiang, Lei Sun, Zhenqiang Ma, Jian Xu, Ryan Pate, Adrienne Stiff-Roberts, Gail J. Brown, Weidong Zhou. Direct measurement of spectrally selective absorption enhancement in Fano resonance photonic crystal cavities on plastic substrates, Photonic and Phononic Crystal Materials and Devices X. 2010/01/26 00:00:00, San Francisco, California, USA. : ,

2012/01/23 1 39   Jian Xu, Zhanao Tan, Chunfeng Zhang, Fan Zhang, Shawn Pickering, Andrew Y. Wang. Colloidal nanocrystal-based light-emitting diodes fabricated on plastic - Towards flexible quantum dot optoelectronics, 2009 14th OptoElectronics and Communications Conference (OECC). 2009/07/13 00:00:00, Hong Kong, China. : ,

2012/01/23 1 38   Ibrahim Abdulhalim II, Akhlesh Lakhtakia, Amit Lahav, Fan Zhang, Jian Xu. Porosity effect on surface plasmon resonance from metallic sculptured thin films, Nanostructured Thin Films. 2008/08/13 00:00:00, San Diego, CA, USA. : ,

2012/01/23 1 37   Jian Xu, Fan Zhang, Akhlesh Lakhtakia, Sean M. Pursel, Mark W. Horn. Circular polarization emission from an external cavity diode laser, Nanostructured Thin Films. 2008/08/13 00:00:00, San Diego, CA, USA. : ,

2012/01/23 1 36   Jian Xu, Fan Zhang, Akhlesh Lakhtakia, Sean M. Pursel, Michael Gerhold. Circularly Polarized Emission from Colloidal Nanocrystal Quantum Dots Confined in Sculptured Thin Film Based Microcavities, 2007 Conference on Lasers and Electro-Optics (CLEO). 2007/05/06 00:00:00, Baltimore, MD, USA. : ,

2012/01/23 1 35   Fan Zhang, Jian Xu, Ting Zhu, Karthik Sarpatwari, Osama Awadelkarim, S. Ashok. Investigating Charge Carrier Mobilities in Nanocrystal-Polymer Hybrid Photovoltaic Devices, 2007 Conference on Lasers and Electro-Optics (CLEO). 2007/05/06 00:00:00, Baltimore, MD, USA. : ,

2012/01/23 1 34   Fan Zhang, Chunfeng Zhang, Zhanao Tan, Ting Zhu, Jian Xu. Investigating High-speed Modulation Characteristics of Quantum Dots in Red Emitting Quantum Dot-Light Emitting Diodes, IEEE Annual Meeting Conference Proceedings. 2008/05/04 00:00:00, . : ,

2012/01/23 1(26   Suzanne Mohney, Steven C. Price, Karthik Shanmugasundaram, Ting Zhu, Fan Zhang, Jian Xu, J. Ruzyllo, Q. Zhang. Formation of Ultra-Thin Quantum Dot Films by Mist Deposition, 212th ECS Meeting. 2007/10/07 00:00:00, Washington, DC. : ,

2012/01/23 0! 21   Li Chen, Hongjun Yang, Zexuan Qiang, Huiqing Pang, Zhenqiang Ma, Jian Xu, Gail J. Brown, Weidong Zhou. Angle and polarization dependent characteristics of colloidal quantum dot absorption in Fano filters on flexible substrates, Quantum Sensing and Nanophotonic Devices VI. 2009/01/25 00:00:00, San Jose, CA, USA. : ,

2012/01/23 0! 19   Jian Xu, Ting Zhu, Andrew Y. Wang, Qingjiang Sun, Yongfang Li, Yongping Yang, Zhanao Tan. Bright and color-saturated quantum dot light-emitting diodes: new star for next generation displays and solid state lighting, Photonics and Optoelectronics Meetings (POEM) 2009: Solar Cells, Solid State Lighting, and Information Display Technologies. 2009/08/08 00:00:00, Wuhan, China. : ,

   TOTAL: **10**

Number of Peer-Reviewed Conference Proceeding publications (other than abstracts):

(d) Manuscripts

Received   Paper

  TOTAL:

Number of Manuscripts:

Books

Received   Paper

  TOTAL:

Patents Submitted

Light Emitting Apparatus

~~Mist Fabrication of Quantum Dot Devices~~

Patents Awarded

Awards

NSF Faculty Early Career Development (CAREER)   Award, 2009

Rustum and Della Roy Innovation in Materials Research Award, 2009

Graduate Students

NAME	PERCENT_SUPPORTED	Discipline
Jie Liu	0.10	
Shawn Pickering	0.20	
Aaron Todd	0.05	
Jeremy Low	0.05	
Fan Zhang	0.05	
Ting Zhu	0.05	
FTE Equivalent:	**0.50**	
Total Number:	**6**	

Names of Post Doctorates

NAME	PERCENT_SUPPORTED
Chunfeng Zhang	0.30
Guanjun You	0.20
FTE Equivalent:	**0.50**
Total Number:	**2**

Names of Faculty Supported

NAME	PERCENT_SUPPORTED	National Academy Member
Jian Xu	0.15	
FTE Equivalent:	**0.15**	
Total Number:	**1**	

Names of Under Graduate students supported

NAME	PERCENT SUPPORTED	Discipline
Samuel R Wilton	0.20	
James Glickstein	0.20	
Chunyan Li	0.10	
Brittany Hedrick	0.10	
FTE Equivalent:	**0.60**	
Total Number:	**4**	

Student Metrics
This section only applies to graduating undergraduates supported by this agreement in this reporting period

The number of undergraduates funded by this agreement who graduated during this period: 4.00

The number of undergraduates funded by this agreement who graduated during this period with a degree in science, mathematics, engineering, or technology fields:······ 4.00

The number of undergraduates funded by your agreement who graduated during this period and will continue to pursue a graduate or Ph.D. degree in science, mathematics, engineering, or technology fields:······ 3.00

Number of graduating undergraduates who achieved a 3.5 GPA to 4.0 (4.0 max scale):...... 4.00

Number of graduating undergraduates funded by a DoD funded Center of Excellence grant for Education, Research and Engineering:...... 0.00

The number of undergraduates funded by your agreement who graduated during this period and intend to work for the Department of Defense 1.00

The number of undergraduates funded by your agreement who graduated during this period and will receive scholarships or fellowships for further studies in science, mathematics, engineering or technology fields: 0.00

Names of Personnel receiving masters degrees

NAME
Jeremy Low
Aaron Todd
Shwan Pickering
Total Number: 3

Names of personnel receiving PHDs

NAME
Fan Zhang
Shawn Pickering
Ting Zhu
Total Number: 3

Names of other research staff

NAME	PERCENT SUPPORTED
FTE Equivalent:	
Total Number:	

Sub Contractors (DD882)

Inventions (DD882)

Scientific Progress

Technology Transfer

Table of Content

Abstract

The goal of the ARO sponsored project is to develop advanced photonic devices based on surface and composition engineered semiconductor nanocrystals. The PI's laboratory has successfully carried out and exceeded the proposed goals of the project with a series of scientific findings and promising technical results. These achievements can be categorized into two major groups. The first group consists of advances in semiconductor nanocrystal-based photovoltaic technology, including thin film solar cells, luminescent solar concentrators, and photonic absorbers, while the second group is composed of accomplishments in nanocrystal light-emitting-diodes (LEDs), nanolasers, and silicon germanium emitters. Among these achievements are the first demonstration of PbSe nanocrystal photovoltaic devices and planar-mixed heterojunction quantum dot solar cells, the first observation of two-photon absorption induced lasing in semiconductor nanocrystals, the design and fabrication of the first photonic crystal-enhanced nanocrystals infrared LED, the first Monte Carlo simulation of infrared luminescent solar concentrator using nanocrystals fluorophores, and the first demonstration of efficient near-band-edge electroluminescence emission from heavy-metal-free semiconductor nanoparticles. These findings and technical results open up new avenues to developing high-performance, environmentally-friend and mass-producible photonic devices with state-of-the-art colloidal semiconductor technology.

Scientific Progress and Accomplishments

The goal of the ARO sponsored project is to develop advanced photonic devices based on surface and composition engineered semiconductor nanocrystals. The PI's laboratory has successfully carried out and exceeded the proposed goals of the project with a series of scientific findings and promising technical results. The major achievements during the course of the project include:

1. Composition- and Morphology-Dependences of the Performance of Hybrid Solar Cells

In our study, the device performance of the hybrid solar cells containing PbSe NQDs and P3HT polymer were characterized with different NQD weight percentages. At different illumination wavelengths, the short-circuit-currents of hybrid devices response diversely to the variation of the NQD loading, UV-VIS-NIR spectroscopy and TM AFM imaging were employed to study the optical and morphological properties of the nanocomposite films, the results of which were correlated to the I-V characteristics of the hybrid devices to interpret the observed spectral response of the solar cell. It is concluded that the observed intensity-dependences of the photocurrents have revealed the pseudomonomolecular recombination kinetics in the NQD-polymer composite, indicating that the efficiency of the hybrid photovoltaic cells can be enhanced by reducing the potential barriers due to the ligand molecules at the surfaces of nanocrystals.
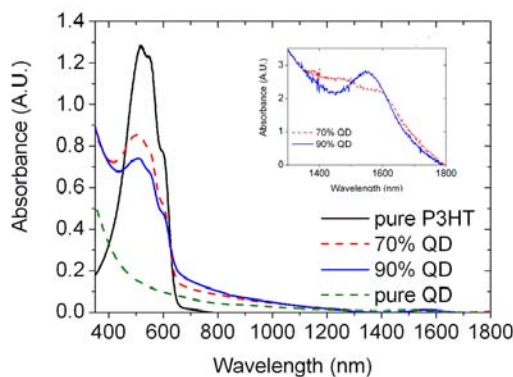

Figure 1: Absorption spectra of a net-P3HT film and two NQD/P3HT blend films with different NQD loadings (70 wt% and 90 wt%). The inset shows the zoomed-in portion of spectra from 1300nm-1800nm, corresponding to the band-gap absorption of PbSe NQDs.

Figure 1 shows the absorption spectra of a net-P3HT film and the NQD/P3HT blend films with two different NQD loadings (70 wt% and 90 wt%). The absorption of the net-P3HT film displays a maximum at 514nm and two vibronic shoulders at 532nm and 560nm, respectively, and cuts off beyond the wavelength of 650nm. There is no noticeable wavelength shift observed

for the absorption maximum in NQD/polymer nanocomposite films except for the substantial drop in the magnitudes. The nanocomposite films, however, exhibit considerable absorption in the near infrared range of the spectrum, which tails to ~1650nm, the absorption cut-off of 6nm-PbSe NQDs. The absorption spectrum of the blended film appears to be a linear superposition of the absorption spectra of the constituent NQDs and the polymer, suggesting that there is no ground-state interaction between the two.
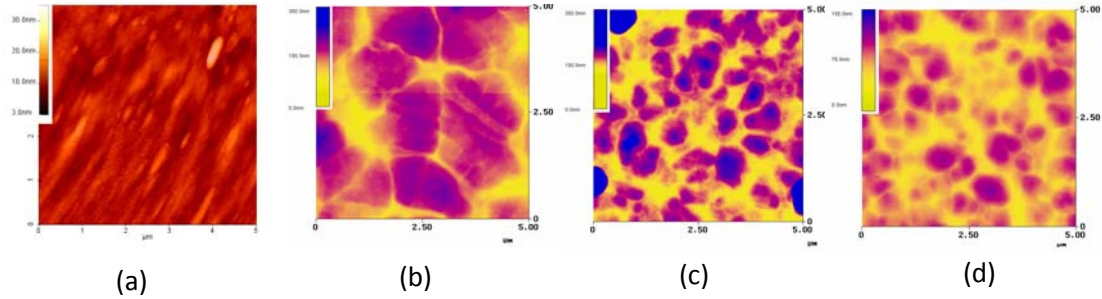

| (a) | (b) | (c) | (d) |

Figure 2: TF AFM images of PbSe NQD/P3HT nanocomposite films of (a) 0 wt% , (b) 70 wt%, (c) 80 wt%, and (d) 90 wt% NQD weight percentages showing different room-mean-square (rms) roughness and phase separation in surface textures.

TM-AFM imaging was performed to study the surface morphology of the nanocomposite films. Figure 2 shows the images (5μm×5μm) of the four films of varied NQD loadings (0 wt%, 70 wt%, 80 wt%, and 90 wt%). The net-P3HT film exhibits a smooth surface with a root-mean-square (RMS) roughness of ~3 nm, as shown in Fig. 2(a) In contrast, the blend films (Fig. 2(b)-(d)) exhibit topographical features of large-scale phase separation with surface textures varying dramatically with composition. At high PbSe-NQD loadings, the film surfaces comprise "island-like" clusters, the height of which could exceed 50nm. Although the composition of the clusters can not be resolved solely by the AFM, it is plausible to identify the clusters as P3HT-rich regions from the fact that the area of the clusters shrinks with the increased NQD/P3HT ratio (Fig. 2(b), (c) and (d)). The severe agglomeration of the P3HT-rich regions and the resulted large scale phase separation as well as the high surface roughness in blend films of 70wt% NQD-loadings can be attributed to the insufficient nanocrystal diffusion in the P3HT polymer matrix, as shown in Fig. 2(b). When the NQD-loading in the blend film approaches 80 wt% or above, those P3HT-rich regions break into many smaller volumes following the appropriate heat treatment, leading to the submicron-scale phase separation between PbSe NQDs and the P3HT polymer in the nanocomposite, as shown in Fig. 2(c) and (d). It is worth noting that the RMS roughness of the blend film reaches 28.8nm and 28.4nm for NQD loadings of 70wt% and 80wt%, respectively, and then dramatically decreases to 15.6nm for the 90wt%-NQD loading. The reduction of the surface roughness can be correlated to the aforementioned evolution of phase separation with the increasing NQD concentration in blend films.

Fig. 3(a) shows the results of the photocurrent characterization for hybrid solar cells of different

NQD loadings upon the monochromatic photoexcitation at 532nm and 808nm, respectively. In the hybrid composite, the absorption cut-off wavelengths of P3HT polymer and 6nm-PbSe NQDs are 650nm and 1550nm, respectively. In the figure the weight percentage (wt %) of PbSe NQDs in the polymer matrix varies between 70-90 wt%. It is found that a high loading of PbSe NQDs ($\geq$70 wt%) in the composite is critical for the effective generation of short-circuit photocurrent from the hybrid device. The short-circuit photocurrents reach the maximum values for both illumination wavelengths in the device containing 80wt% PbSe NQDs. The hybrid solar cell exhibits diverse photoelectric responses to the visible and NIR wavelengths upon the
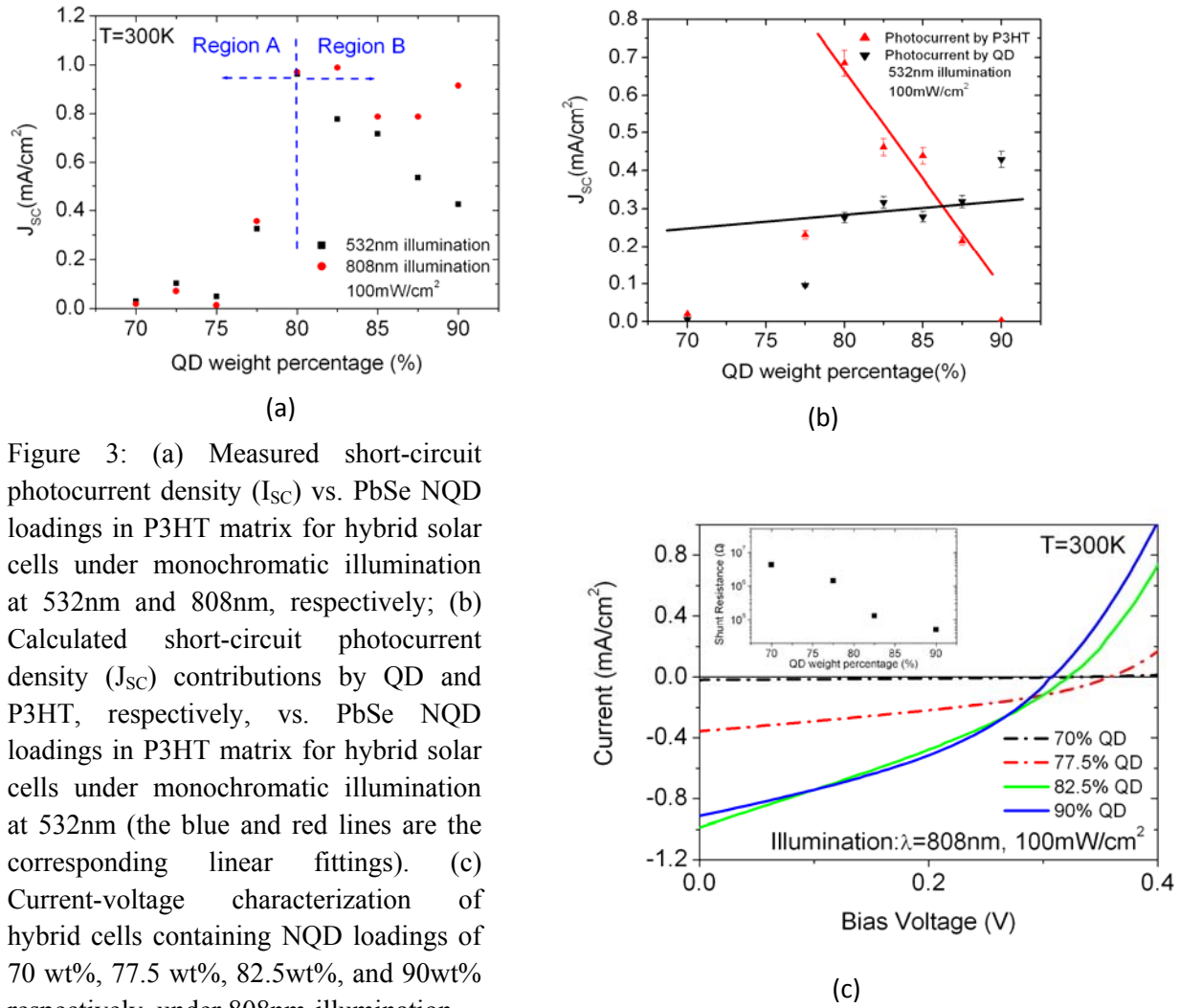

(a)

(b)

Figure 3: (a) Measured short-circuit photocurrent density (I_{SC}) vs. PbSe NQD loadings in P3HT matrix for hybrid solar cells under monochromatic illumination at 532nm and 808nm, respectively; (b) Calculated short-circuit photocurrent density (J_{SC}) contributions by QD and P3HT, respectively, vs. PbSe NQD loadings in P3HT matrix for hybrid solar cells under monochromatic illumination at 532nm (the blue and red lines are the corresponding linear fittings). (c) Current-voltage characterization of hybrid cells containing NQD loadings of 70 wt%, 77.5 wt%, 82.5wt%, and 90wt% respectively, under 808nm-illumination.

(c)

further increment of the NQD concentration: the short-circuit photocurrent retains high under NIR illumination (λ=808nm) while the photocurrent produced by 532nm-illumination degrades significantly. When the NQD loading approaches 90 wt%, the light-harvest efficiency at 532nm-wavelength drops by 55% with respect to the maximum value.

The objective of the selective photoexcitation study on the hybrid cells is to comprehend the spectral contributions of different light-harvest components in hybrid devices, which is essential for designing efficient solar cells. By inspecting the light-absorption properties of P3HT and PbSe NQDs in Figure 1, it is evident that, under near infrared (NIR) illumination (λ=808nm), excitons were only created in PbSe NQDs in the solar cell, which accounts for the high short-circuit photocurrent under NIR illumination for NQD loadings above 80 wt%. Upon 532nm-photoexcitation, we, however, expect exciton contributions from both P3HT and PbSe NQDs in the hybrid device because both components absorb light of wavelength below 650nm. In our study, the measured short-circuit-current under NIR illumination was used to extract the photocurrent response of PbSe NQDs to the light of shorter wavelength. Since the absorption spectrum of the nanocomposite film was found to be a linear superposition of the absorption spectra of the constituent NQDs and the polymer, the fractions of the 532-nm light absorbed by the nanocrystal and polymer, respectively, can be determined accurately by calculating the volumetric ratio of the two components in the film. By assuming a constant internal quantum efficiency for the photoelectric responses of PbSe NQDs at the two illumination wavelengths (532nm and 808nm), one can calculate the photocurrent produced by PbSe NQDs and consequently differentiate the spectral contributions of the two components in the hybrid device upon 532nm-photoexcitation:

$$\frac{J^{QD}_{808nm}}{P^{QD}_{808nm}*808} = \frac{J^{QD}_{532nm}}{P^{QD}_{532nm}*532}$$

where J^{QD}_{808nm} & J^{QD}_{532nm} are short-circuit-currents produced by PbSe NQDs under 808nm-illumination and 532nm-illumination, respectively, and P^{QD}_{808nm} & P^{QD}_{532nm} are the incident light power absorbed by NQDs under 808nm-illumination and 532nm-illumination, respectively.

In Fig. 3(b), the short-circuit-photocurrents, J^{QD}_{532nm} and J^{P3HT}_{532nm}, contributed by the nanocrystal- and polymer-components in the hybrid solar cell were determined by Eq. (1) and plotted as functions of NQD loadings. When the NQD loading varies between 80-87.5 wt%, there is a nearly linear growth of J^{QD}_{532nm} with the weight percentage of NQDs in the nanocomposite, while J^{P3HT}_{532nm} decreases with a greater slope over the same range of NQD loading, indicating the absorption-dependence of the light harvest process in hybrid solar cells. Noteworthy is the fact that photocurrent produced by the polymer matrix under 532nm-illumination counts ~65% of the overall photocurrent even at high NQD loadings up to 85 wt% due to the much larger absorption cross-section of the conjugated P3HT polymer than that of PbSe nanocrystals at short wavelengths (Figure 1) as well as the low mass-density of the polymeric material.[1] The decreased volume fraction of P3HT in the hybrid solar therefore explains the observed reduction of the overall photocurrent under 532-nm illumination when the loading of PbSe NQDs was raised in the nanocomposite.

The linear relationship between the photocurrents and NQD ratios, however, does not hold for the NQD loadings below 77.5 wt% and above 90 wt%, as shown in Fig, 1(b). We speculate that the observed discrepancy can be traced back to the structural and morphological properties of the hybrid solar cells. Apart from the light absorption, there are other limiting factors for the efficient light-harvest in bulk heterojunction photovoltaic devices, including the phase separation and the percolation pathways for charge carrier transport. Since the PbSe NQDs (6nm) and the P3HT forms a type-II heterojunction at their interfaces, charge separation is favored between the high electron-affinity inorganic semiconductors and the low ionization-potential polymer.[2] In PbSe NQD/P3HT solar cells, the need for submicron-phase-separated polymer-NQD blends is therefore expressed by the limiting exciton diffusion length present in organic and nanocrystal semiconductors. Upon the charge separation at NQD/polymer interfaces, PbSe NQDs will accept electrons and transport them to the Al electrode through the nanocrystal network by hopping or tunneling process, while P3HT will accept holes and transport them to the transparent PEDOT/PSS-indium tin oxide (ITO) electrodes.[3,4,5,6,7,8] The effective charge transport relies on the development of the interpenetrating networks of the acceptor (P3HT) and donor (PbSe NQD) materials within these blend films.

Since the typical distances that photo-excitons travel within the polymer matrix are in the submicron or nanometer scale,[4] the relatively large scale phase separation observed in the TM AFM image of the 70wt%-NQD blend film (Fig. 2(b)) can therefore account for the measured low short-circuit photocurrents. In the blend film containing 80wt% or more NQDs, the observed submicron-phase separation (Fig. 2(b)) leads to the dramatic increase of the photocurrent for both illumination wavelengths, as shown in Figure 3. When the loading of PbSe NQDs rises beyond 90 wt%, there is, however, an insufficient amount of P3HT in the film, which resulting in the reduced absorption at 532nm as well as the degraded hole-transport in the solar cell, both of which, in turn, hinder the production of photocurrents by the P3HT component of the film under 532nm-illumination. Since the infrared light is absorbed by PbSe NQDs, the photocurrent produced by the infrared illumination does not decrease at high NQD loadings.

Fig. 3(c) plots the I-V curves of hybrid solar cells containing NQD loadings of 70 wt%, 77.5 wt%, 82.5wt%, and 90wt% respectively, under NIR illumination (λ=808nm). It is observed that the open circuit voltage (V_{OC}) drops with the increasing loading of NQDs in the composite. A plausible explanation on the NQD-dependence of V_{OC}'s could be related to the formation of shunt paths in the solar cell composites. As the loading of PbSe NQDs increases in the composite film, a large amount of electron-conducting nanoparticles are in contact with the hole-collecting electrode of the PEDOT: PSS/ITO bilayer, which tends to create effective shunt paths for free carriers in the bulk heterojunction structure and reduce the open circuit voltage of the solar cell. We have measured the I-V characteristics of devices in the dark and calculated the shunt resistances at zero bias. The shunt resistance decreases at higher NQD loading, as shown in the inset of Fig. 3(c), which is consistent with the observed reduction in open-circuit photovoltage.

Under 100mW/cm^2-illumination, the measured short-circuit photocurrents, for the device of 80wt%-NQD loading, are 0.97mA/cm^2 for 805nm-light and 0.96mA/cm^2 for 532nm-light, respectively. The incident monochromatic photon to current conversion efficiencies (IPCE's) for 808nm and 532nm were calculated as 1.34% and 1.0%, respectively. The short-circuit internal-quantum-efficiency (IQE) of the same device reaches 21% when the net absorption of 6.4% of the incident NIR light in the NQD/polymer composite film is taken into consideration. The net absorption was determined by directing the NIR beam (100mW/cm^2) into the photovoltaic cell and measuring the reflection-off of the mirror-like Al-electrode of the device, and the data has been corrected for the surface reflection from the front and back sides of the ITO glass substrate. In contrast, the IQE for 532nm-wavelength is only 5%, indicating that the inferior light-harvest efficiency at shorter wavelengths in the solar cell.
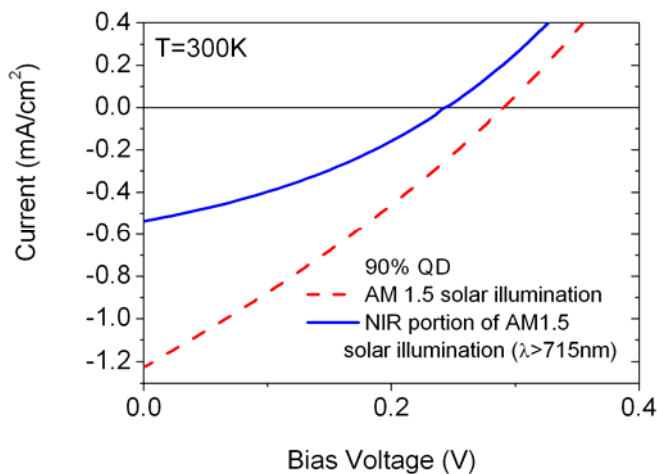

Figure 4: Current-voltage characterization of the NQD-P3HT based hybrid solar cell under the illumination of an AM1.5 solar simulator.

The photovoltaic response of device under 1-sun AM1.5 illumination is plotted in Figure 4. For the device containing 90wt %NQDs, the measured short-circuit current is 1.21mA/cm^2; the open-circuit voltage is 0.30V; the filling factor is determined as 0.34. The calculated power conversion efficiency (PCE) is only 0.15%. In order to investigate the contribution of the NIR response of NQDs in the photovoltaic signal of the device, a long pass-filter with 715nm-cutoff wavelength was employed to illuminate the device with only the NIR-portion of the solar energy. The measured short-circuit current is 0.52 mA/cm^2 under infrared part of solar illumination, which amounts to 43% of the entire photocurrent response of the hybrid device, whereas the open-circuit voltage declined slightly from 0.30V to 0.24V upon NIR illumination.

The intensity dependences of the photocurrents were measured and plotted in Figure 5. Under reverse bias condition (-0.5V), the power-law-analysis on the photocurrent-excitation power relationship reveals an exponent of 1.08 within the range of experimental error. The short circuit current exhibits a similar linear intensity dependence, but with a smaller amplitude. The linear intensity dependence of the photocurrent is indicative of a pseudomonomolecular recombination

7

kinetics, meaning the density of trapped charges in the NQD-P3HT composite is comparable to the free carrier density[9,10,11] It has been reported that, in colloidal semiconductor NQDs, the trapped electron- and hole-carriers tend to reside at the surface states of nanocrystals, the capping ligands, some radical species such as $SeO2^-$ or $O2^-$, as well as some uncommon defects or impurities.[6,7,8] Since the "as grown" PbSe NQDs applied in this study were overcoated with the 2nm-length oleate ligands, it is suspected that these long capping molecules pose a barrier for the transport of photo-carriers at the surface of the nanoparticle surfaces, and lead to the large amount of trapped charges in the active region, which substantially limits the power conversion efficiency of the hybrid photovoltaic device under study. Sargent *et al* have demonstrated that, by conducting the ligand exchange at nanocrystal surfaces to replace oleate ligands with shorter chain alkyl amine, the efficiencies of the NQD-based light emitting devices and photovoltaic devices can be enhanced significantly.[12] Techniques to ligand-exchange the PbSe NQDs are currently under investigation. It is expected that surface-engineered PbSe NQDs could potentially facilitate the charge separation and enhance the carrier transport at NQD-polymer interfaces for higher power conversion efficiency.
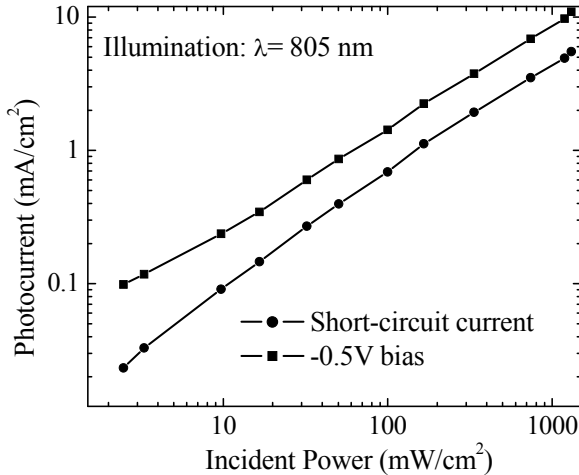

Figure 5: Reverse bias photocurrent and short-circuit current as functions of incident power.

2. Integration of Planar and Bulk Heterojunctions in Polymer/Nanocrystal Hybrid Photovoltaic Cells

We have utilized the ligand-capped PbSe quantum dots (QDs) to construct planar-mixed heterojunction (PM-HJ) solar cells with a new solution-processing technique. The device has been configured with a multilayer structure: ITO (indium tin oxide)/(Poly(3,4-ethylene dioxythiophene) :poly(styrene sulphonate))/P3HT/P3HT:PbSe/Ca-Al. Under infrared irradiation (808nm, 100mW/cm^2), the PM-HJ cell produced an open-circuit voltage (V_{oc}) of 0.38 V, a short-circuit current density (J_{sc}) of 1.73 mA/cm^2, a filling factor (FF) of 40%, and an overall power

8

conversion efficiency (PCE) of 0.26%, representing a significant improvement in performance over many existing infrared cells reported hitherto. In a parallel effort, we have investigated the coupling of PbSe colloidal QDs, with peak emission at 1.55μm, to silicon two-dimensional photonic crystal microcavities. The QDs were positioned within a small air hole at the center of the microcavity. Significant enhancement of spontaneous emission, with a sharp resonance peak at 1.55 μm corresponding to a Q factor of 775, was observed for single defect H2 microcavities. The measurement results matches well with the calculated Purcell factor (~35) and spontaneous emission coupling factor (0.04), respectively.

We have recently utilized the ligand-capped PbSe QDs to construct multilayer PM-HJ solar cells with a new solution-processing technique. The devices were configured with a multilayer structure: ITO (indium tin oxide)/PEDOT:PSS (Poly(3,4-ethylene dioxythiophene) :poly(styrene sulphonate))/P3HT/P3HT:PbSe/Al. For the sake of comparison, we have also fabricated Bulk-HJ device with the structure of ITO/PEDOT:PSS/P3HT:PbSe/Al as the control device. Under infrared irradiation (808nm, 100mW/cm^2), the Bulk-HJ cell produced an open-circuit voltage (V_{oc}) of 0.25 V, a short-circuit current density (J_{sc}) of 1.10 mA/cm^2, a filling factor (FF) of 35%, and an overall power conversion efficiency (PCE) of 0.12%. The PM-HJ like cells showed a significant improved performance among the best infrared solar cells reported hitherto, with V_{oc} increased to 0.38 V, J_{sc} greatly increased to 1.73 mA/cm^2, FF increased to 40%, and PCE reached 0.26%, which is nearly three times higher than the Bulk-HJ cell.
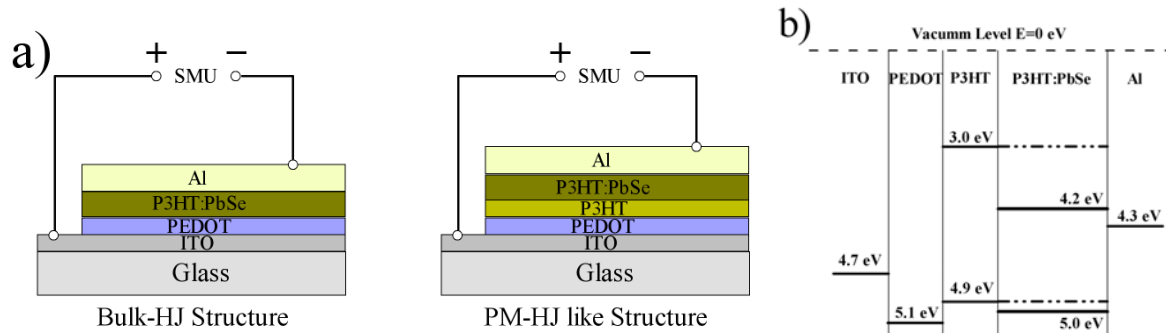

Figure 6. a) Device structure of bulk-HJ cell and PM-HJ like cell; b) energy level diagram of the PM-HJ like PbSe-P3HT based hybrid solar cell; c) room temperature absorption and photoluminescence spectrum of PbSe QDs dispersed in terachloroethylene solvent (inset: high resolution transmission electron microscopic image of a 6 nm PbSe quantum dot).

Figure 6a shows schematically the structure of a photovoltaic cell with bulk-HJ structure and a cell with PM-HJ like structure respectively. The bulk-HJ cell was created by employing PbSe QDs blended with P3HT. To enhance the charge transport capabilities, a PM-HJ like cell was fabricated by inserting a thin layer of P3HT (~20 nm) between the ITO/PEDOT (~30 nm) anode and P3HT: PbSe blended active layer (~50 nm). The peak absorption of P3HT is in the visible region of the spectrum, whereas the absorption of PbSe QDs is tailored to cut off in the near infrared region. In the device, photocarriers will be generated in P3HT and PbSe QDs upon absorption of both the visible and the infrared portions of the solar radiation.

A simplified energy band diagram of the device is depicted in Figure 6b. The illustrated band-gap energy of PbSe QDs is estimated from the measured lowest excitonic absorption peak. It has been assumed that the conduction and valence bands in the nanoparticle shift by the same energies relative to the bulk material due to the nearly equal effective masses for holes and electrons in PbSe. Since the lowest unoccupied molecular orbital (LUMO) and the highest occupied molecular orbital (HOMO) of P3HT lie above the conduction-band (CB) and Valance-band (VB) edges of PbSe QDs respectively, the PbSe:P3HT composite forms a type-II heterojunction at the QD/polymer interface. Charge separation is therefore favored between the high electron-affinity inorganic semiconductors and the low ionization potential polymer. The ionization potential energy of PEDOT:PSS is close to that of P3HT to minimize the hole extraction barrier at the anode surface.
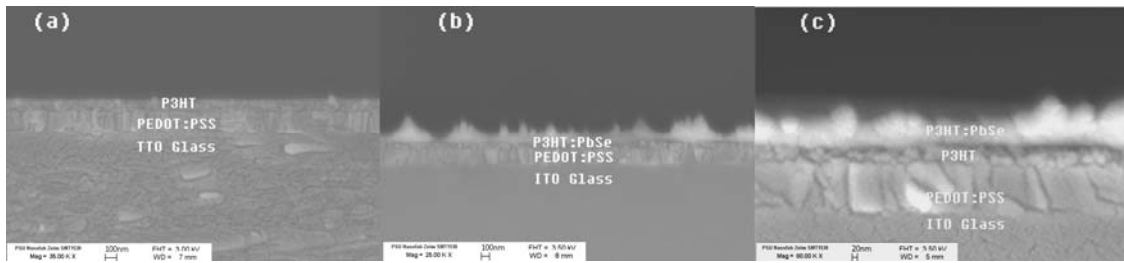

Figure 7: Cross-sectional SEM images of P3HT, P3HT:PbSe, and P3HT/P3HT:PbSe spin-coated on the ITO/PEDOT electrode.

The interface of P3HT/P3HT:PbSe has been investigated by conducting the cross-sectional scanning-electron-microscopy (SEM) imaging of the fabricated photovoltaic cells, as shown in Fig. 7. Figure 7(a) and (b) show the cross sections of the P3HT and P3HT:PbSe spin-coated on the ITO/PEDOT:PSS surface respectively. A sharp interface is observed with the estimated thickness of PEDOT:PSS, P3HT and P3HT:PbSe as ~ 80 nm, 25 nm and 50 nm, respectively. The thicknesses of P3HT and P3HT:PbSe are very critical in designing the PM-HJ solar cells: The thickness of P3HT should approximate to the thickness of exciton diffuse length in P3HT:PbSe, and the thickness of P3HT:PbSe should be less than a characteristic parameter referred to as the carrier collection length in order to alleviate the charge collection bottle-neck in the resistive blended layer. Figure 2c clearly reveals the interfaces of P3HT:PbSe/P3HT and P3HT/PEDOT:PSS. The thickness of P3HT remains unchanged as Figure 2(a), indicating that, upon spin-coating the upper layer of P3HT:PbSe, the underneath P3HT layer was not dissolved by the solution. The observed robustness of the underneath P3HT layer can be attributed to two major factors: (1) P3HT is a region-regular polymer. At an elevated temperature, the hexyl on the thiophene ring can rearrange to a certain direction, the directional side-chain protected the main-chain unresolved by the solution. (2) The long chain ligand of oleic acid over the surfaces of PbSe QDs greatly changed the solubility property of P3HT:PbSe solution at a high PbSe loading.

Figure 8 plots the *J-V* characteristic of the infrared photovoltaic cells based on the bulk-HJ structure and PM-HJ like structure in the dark and under illumination (808nm, 100mW/cm^2) conditions. The *J-V* curves measured in the dark shows a rectification ratio of 15 for the bulk-HJ structure, while 92 for the PM-HJ like structure. The higher rectification ratio of the solar cell with PM-HJ structure results from the high injection current at forward bias and lower leakage current at reverse bias and, at the same time, a significantly reduced recombination current in the depletion region.

Under IR illumination, the device based on the PM-HJ structure shows improved photovoltaic performance as shown in Fig. 3b. The device with bulk-HJ structure shows V_{oc} of 0.25 V, J_{sc} of 1.10 mA/cm^2, FF of 35%, and PCE of 0.10%, consistent with our early results. Importantly, the V_{oc}, J_{sc}, FF, and PCE of the PM-HJ structured device increased altogether and reached 0.38 V, 1.73 mA/cm^2, 40%, and 0.26%, respectively, which are among the best values reported in literatures for the infrared solar cells based on P3HT and PbSe. By introducing P3HT planar layer into the PM-HJ like structure, the efficiency of the device was raised by ~3 times. The observed improvement can be explained by the reduced mobility in the mixed D-A layer: the carrier drift length in an electric field before recombination may be comparable to or less than the mixed layer thickness, leading to incomplete collection of photogenerated charges at the electrodes. Charge transport in the homogeneous layers is considered to be lossless as photogenerated holes and electrons are spatially separated unless the applied voltage approaches the built-in potential.
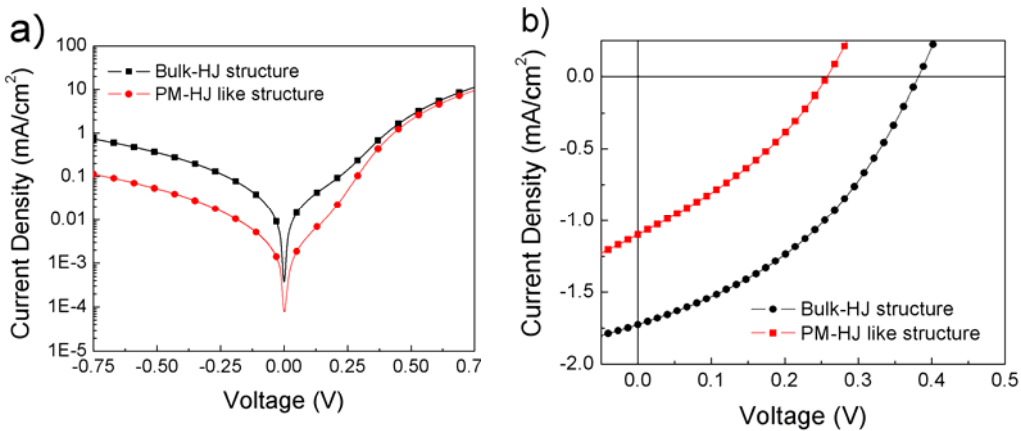

Figure 8: J-V curves of infrared solar cell based on bulk-HJ structure and PM-HJ like structure in the dark (a) and with 808 nm laser illumination at 100 mW/cm^2 (b).

The current density-voltage characteristic (*J-V*) of the infrared solar cell based on PM-HJ like structure under different illumination intensities P_{light} at λ=808 nm is shown in Figure 9, the inset of which also plots the J_{sc} as a function of P_{light}. The photocurrent is primarily due to exciton dissociation at the donor-acceptor (D-A) interface and the subsequent transport of charge carriers

to the respective electrodes, which is almost bias independent except at a very high forward bias voltage, whereby the external electric field may inhibit the transport of photogenerated carriers to the electrodes. The series and shunt resistances of the working devices degraded from low to large light intensities owing to the poor charge transport (hopping) behavior in QDs. As shown in the inset, $\ln(J_{sc})$ increases logarithmically with incident light intensity, and the J_{sc} follows the power-law dependence with a power factor of 0.93: $J_{sc} \sim P_{light}^{0.93}$. The nearly linear dependence of the J_{sc} indicates that charge-carrier losses in the absorber bulk are dominated by monomolecular recombination. This is in agreement with the picture of photogeneration and transport of charge carriers in a PM-HJ like structure: an ultrafast electron-hole separation is followed by the transport of negatively and positively charged carriers within spatially separated networks, that is, electrons travel in percolated QDs towards the Al contact while holes pass through the polymer P3HT matrix and the P3HT planar layer towards the PEDOT: PSS/ITO contact. As both contacts may be considered ohmic for the respective charge carriers, no sparse charge is formed under short-circuit conditions.
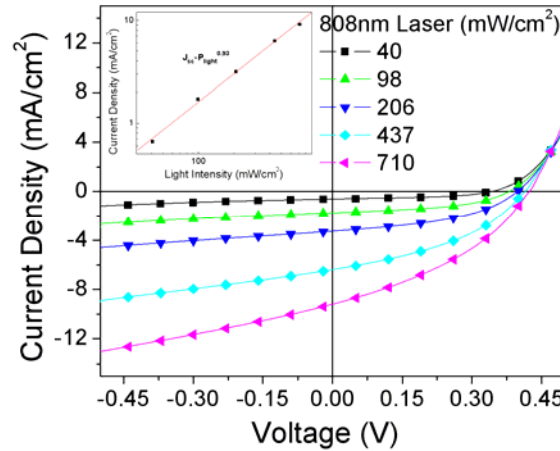

Figure 9. J-V characteristics of infrared solar cell based on PM-HJ like structure at different incident light intensities with an 808 nm laser illumination. Inset: Short-circuit current density (J_{sc}) as functions of light intensity.

Noteworthy is the observation that the PCE of the photovoltaic cell based on PM-HJ like structures only drops slightly (~0.19%) at high illumination intensities up to 710 mW/cm^2. This makes it possible to use the hybrid photovoltaic cells with the solar concentrators for enhanced light harvest efficiencies.

3. Electroluminescence from Silicon-Based Photonic Crystal Microcavities with PbSe Quantum Dots:

Several technologies are currently being investigated to realize a silicon complementary metal oxide semiconductor (CMOS)-compatible lightwave network for inter- and intra-chip optical interconnects. A key requirement is an on-chip integrated laser that can preferably emit at wavelengths ~1.3-1.6 μm. Hybrid technologies such as wafer bonding and direct growth of III-V semiconductor quantum dot lasers on silicon have been demonstrated. One of the more promising approaches is to employ chemically synthesized nanocrystals such as Pb(S, Se) and CdSe colloidal quantum dots (QDs) as the gain media and couple their emission to the resonances of suitable high quality-factor (high-Q) microcavities. In this context, these nanocrystals have been coupled to various types of resonant cavities formed in photonic crystals, toroidal microcavities , photonic beads, silicon-on-insulator (SOI) membranes, and glass capillaries to demonstrate amplified spontaneous emission and lasing. The recently developed PbSe colloidal QDs provide size tunable interband absorption and emission in a broad wavelength range spanning 0.8-4.0 μm, and have a high photoluminescence (PL) efficiency of ~89%. [13] Using nanocrystal-microcavity coupling, lasing has been demonstrated by optical pumping. For a more compact and versatile light source on a silicon platform, an *electrically* injected laser is desired. To realize an electroluminescent device, it is necessary to link the QDs immersed in a conjugated polymer matrix with suitable charge transport layers. Additionally, if lasing is desired, then the electroluminescence has to be coupled with a high-Q cavity. In this letter, we demonstrate electrically injected enhanced spontaneous emission from PbSe QDs coupled to silicon photonic crystal (PC) microcavities wherein the coupling of the QD emission with the microcavity resonances can be clearly observed.

PbSe QDs are chemically synthesized by a non-coordinating solvent technique. By carefully controlling the growth conditions, highly monodispersed PbSe QDs are produced without any precipitation. The final nanocrystals are stabilized with a capping layer of oleate molecules coordinated to the Pb atoms.

In order to fabricate a device suitable for electrical injection, PbSe colloidal QDs are mixed with poly[2-methoxy-5-(2'-ethyl-hexyloxy)-1,4-phenylene vinylene] (MEH-PPV), a conductive polymer matrix, and sandwiched between an indium tin oxide (ITO) anode and a thermally evaporated top cathode consisting of tris(8-hydroxyquinoline)aluminum (Alq$_3$), calcium, and aluminum. The device heterostructure is schematically shown in Fig. 10(a). The ITO surface is altered by a layer of poly(3,4-ethylenedioxythiophene) poly(styrenesulfonate) (PEDOT:PSS), the purpose of which is two-fold: to make it smooth to prevent electrical shorts, and to align the Fermi level of ITO with the hole state of PbSe QDs as closely as possible for the efficient hole injection (Fig. 10(b)).
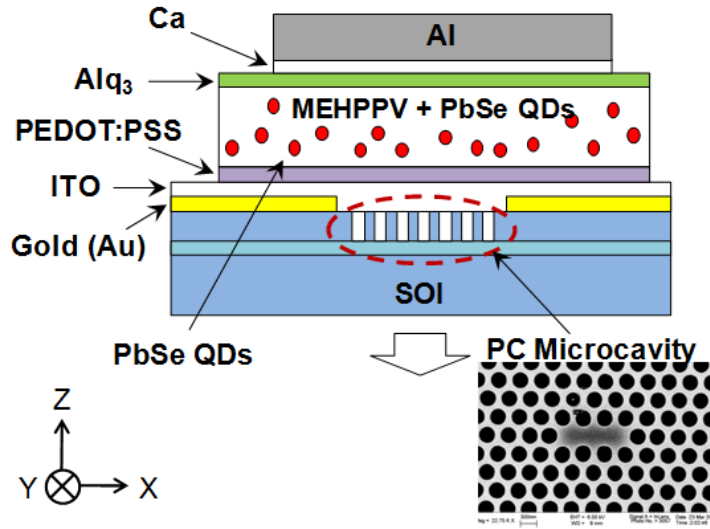
(a)
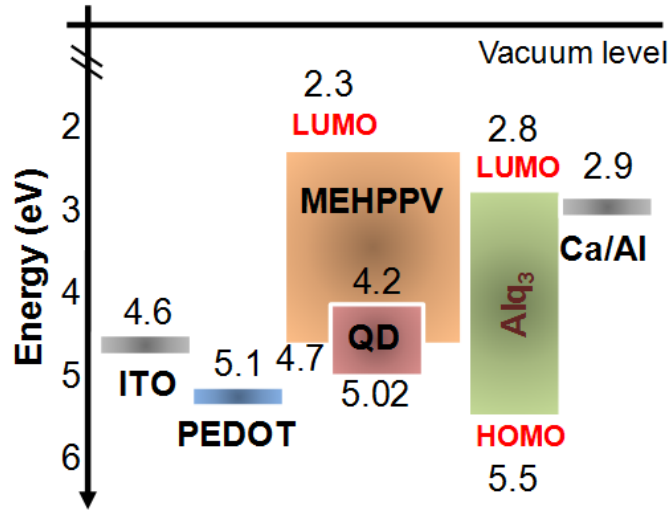
(b)

Figure 10 (a) Schematic of the device heterostructure fabricated on silicon-on-insulator (SOI). PbSe quantum dots with MEH-PPV are clad by PEDOT:PSS on the ITO anode and Alq₃/Ca/Al cathode. The inset is a SEM image of the L3 defect photonic crystal microcavity in silicon. Outer air holes at both edges in the defect are shifted by $0.1a$; (b) energy band diagram of device heterostructure with PbSe quantum dots as a gain medium.

The resonator was designed as an L3 defect PC microcavity with three missing holes in a line in the silicon layer of a SOI wafer. The PC is therefore clad by SiO$_2$ and ITO on the two opposite surfaces. The outer air holes at both edges of the L3 cavity are shifted by 0.1a (The inset of Fig. 10(a)) in order to reduce leaky components of the in-plane electric field and attain a high Q-factor. Since ITO is deposited on the photonic crystal with air holes, it was expected that a small amount of filling of the holes would be unavoidable due to the conformal nature of the deposition. However, as observed by scanning electron microscopy (SEM), the degree of filling is extremely small. The Q-factor and modal volume of the L3 cavities, as estimated from three-dimensional finite difference time domain (FDTD) calculations, are 2,000 and 0.14 μm^3 ($\sim$1.6(λ_c/n)^3), respectively. Asymmetric cladding by SiO$_2$ and ITO, both having refractive indices larger than air (n=1) results in a smaller Q-factor and larger modal volume than the values quoted above with air cladding.

Unlike a regular PC microcavity device, the active gain medium containing the PbSe QDs in this device is spatially separated from the PC resonator by a 200 nm ITO layer. However, this separation is short enough for the light from PbSe QDs to couple to the PC slab since the light wavelength in ITO is $\sim$1.22 μm (corresponding to 1.55 μm in free space). Figure 11 shows the electric field along the z-direction calculated by the transfer-matrix method with the refractive index profile shown (blue solid line). The calculated overlap of the in-plane electric field in the PC slab with the gain medium is $\sim$1%, which is comparable to the confinement factor in single quantum-well lasers and this value is very sensitive to the ITO thickness.

The devices were characterized at room temperature by applying a forward bias between the ITO anode and the Al cathode. The light output from the device was analyzed with a 0.75 m high-resolution spectrometer and detected with an InGaAs photomultiplier tube using phase lock-in amplification. The output spectra of the control device without a PC microcavity exhibit a broad emission between 1.4-1.7 μm, with a full-width-at-half-maximum (FWHM) of $\sim$180 nm (Fig. 12(a)). On the other hand, as shown in Fig. 12(b), the room temperature spectral output of the device with a PC microcavity exhibits a distinct resonance at λ=1669 nm with a linewidth of $\sim$4 nm at an injection current of 8 mA (a current density of 113 mA/cm^2), which corresponds to a cavity Q factor of $\sim$420. The measured current-voltage (I-V) characteristic of the device is shown in the inset. In contrast to the control device, the device with a PC microcavity has a 1,000 times smaller active area ($\sim$6.4×10^{-3} mm^2); hence the broad background light is not seen. We believe that the light from the active gain medium is not perfectly coupled and guided in the PC slab because of their spatial separation. This results in a lower value of Q than calculated. With an assumed dot density of 10^{12} /cm^2, $\sim$10^6 carriers are injected into a PbSe QD per second, which implies that it would be impossible to attain stimulated emission. Therefore, the observed resonance is a manifestation of the Purcell effect which enhances the spontaneous emission. The maximum achievable Purcell factor is expressed as $F_C = 3\lambda_c^3 Q / 4\pi^2 n^3 V_{mode}$. With an estimated mode volume of $\sim$1.6(λ_c/n)^3 and a cavity Q of $\sim$420, we estimate F_C to be $\sim$25 in the

electroluminescent devices. Since this is the maximum value theoretically calculated assuming that the gain medium is positioned at the maximum electric field, additional measurements such as time-resolved electroluminescence of PbSe QDs with and without the PC microcavity are required to accurately estimate the enhancement of spontaneous emission.
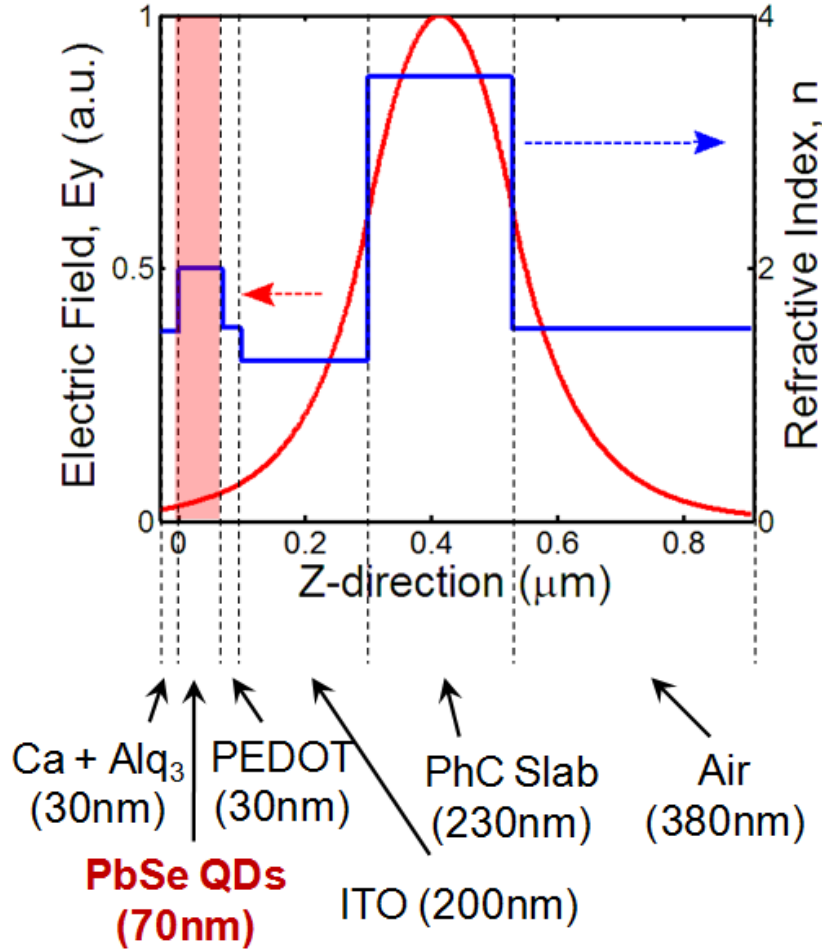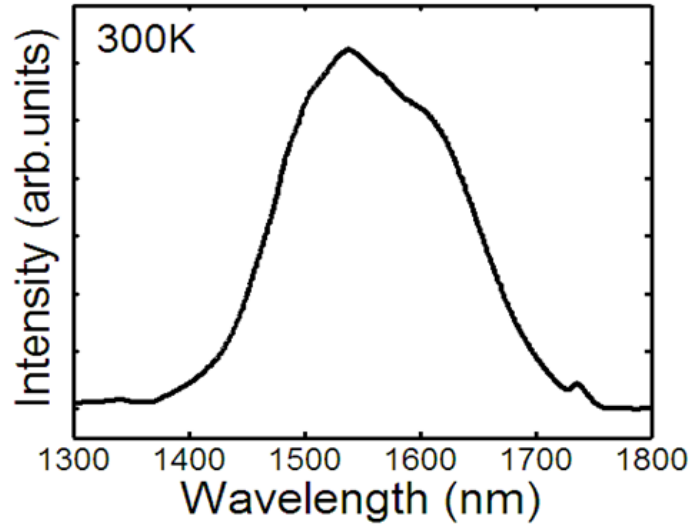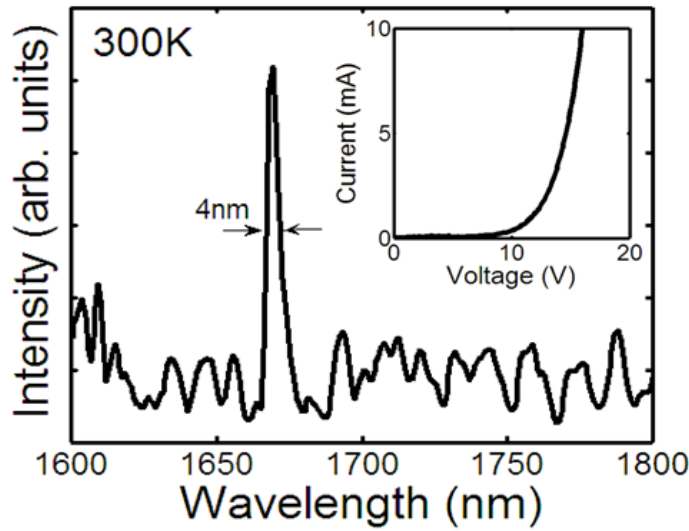

Figure 11: Distribution of the electric field (red solid line) along the z-direction (vertical direction) calculated by the transfer-matrix method with the refractive index profile shown (blue solid line). The shaded area corresponds to the overlap of confined electric field in the PC slab with the gain medium, which is ~1%.

(a)

(b)

Figure 12: (a) Measured room temperature electroluminescence of the control device without a photonic crystal microcavity and a gold blocking layer. The device exhibits a broad emission wavelength between 1.4-1.7 μm with a linewidth of ~180 nm; (b) room temperature electroluminescence spectra from the device with a silicon based PC microcavity with PbSe quantum dots. The resonant mode is observed at λ=1669 nm with a linewidth of ~4 nm. The inset of (b) shows measured current-voltage characteristics of a fabricated device with a turn-on voltage of ~12 V.

In order to achieve coherent emission and lasing, the thickness of the ITO layer needs to be carefully optimized and charge transporting layers which can withstand higher current densities need to be identified and characterized. It is also worth mentioning that the PbSe QDs used in this study are coated with a layer of long-chain oleate ligand for passivation of surface states, but this ligand functions as a barrier to impede the carrier transport between PbSe QDs and the host matrix. To alleviate this problem, the use of PbS/PbSe core-shell nanocrystals for ligand exchange [10] should be investigated for enhancing the radiative efficiency of PbSe QDs.

To summarize, we demonstrate enhanced spontaneous emission at room temperature from electrically injected silicon photonic crystal microcavities with PbSe QDs as the gain media. With a current density of 113 mA/cm^2, a resonance at λ=1669 nm having a linewidth of 4 nm is observed, which corresponds to a cavity Q factor of ~420. For better device performance, it is essential to optimize the ITO layer thickness and improve the characteristics of the electron and hole transporting layers. This nanoscale light sources based on silicon, which is capable of being fabricated on CMOS chips, is of interest as a practical technology for optical interconnects in silicon photonics.

4. Two-photon pumped self-lasing in semiconductor nanowires and nanodisks:

The emergence of high quality 1D and 2D compound nanostructures, such as Zn(O,S) and GaN nanowires and nanodisks, has spurred a great interest of exploring the self-lasing actions in those natural resonance cavities since 2001. Owing to the high refractive index difference between the compound materials and the surrounding dielectric environment, those nanostructures act as fiber or slab waveguides to support axially guided modes or Whispering Gallery modes for self-lasing at low thresholds and high Q-factors. The effort to achieve two-photon pumped self-lasing in these nanostructures allows for the replacement of deep-UV excitation with visible or near-IR light pumping, which will greatly extend the application of those nanolasers in integrated nanophotonic circuitry, on-chip chemical sensing, biomedical diagnostics and phototheraphy.

Our recent acquisition of the femtosecond amplifiers with the ARO DURIP award has allowed the PI's group to investigate the two-photon absorption (TPA)-induced self-lasing in a variety nanostructures of II-VI and III-V compounds, including ZnO, ZnS, and CdSe nanorods/wires as well as ZnO and CdSnS nanodisks. Figure 13 shows the emission spectra of ZnS nanowires (90nm-diameter) and ZnO nanodisks (100nm-thick), respectively, upon two-photon excitation at λ=532nm and λ=700nm, respectively. In both cases the threshold behaviors were confirmed by the observed evolutions from the broadband spontaneous emission to the sharp lasing modes as illustrated in the output spectra. Also presented in the insets are the transmission-electron-microscopy (TEM) images of the nanostructures and the far-field output emission patterns.

The lasing modes and output emission patterns have shown strong dependence on the nanostructure geometry and dimensions. Multiple longitudinal modes were resolved for the stimulated emission of ZnS nanowires, with the dominant mode, peaked at 320nm, exhibiting a narrow linewidth of ~ 0.8 nm. The minimum mode spacing is ~2nm, which is consistent with the ~10μm-length of the ZnS nanowire cavity under investigation. The well-defined end facets of the nanowire provide the necessary reflectance for the cavity resonance. On the other hand, the far-field output image of the ZnO nanodisk clearly portrays the Whispering Gallery lasing modes in the ZnO nanodisk. The wavelengths of the two lasing peaks observed in the nanodisk output spectrum represent nearly perfect matches to the transverse magnetic (TM) modes of orders 93 and 94 for the 3μm-diameter (vertex to vertex) hexagonal nanodisk.
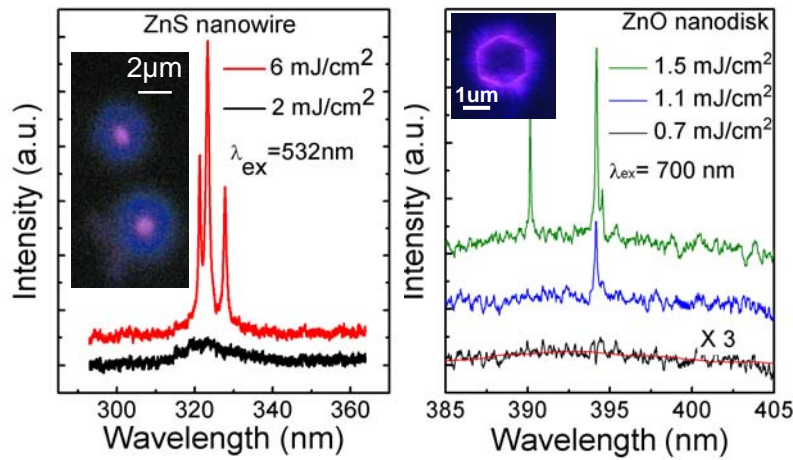

Figure 13: Two-photon pumped self-lasing spectra from a ZnS nanowire (left) and a ZnO nanodisk (right), respectively. The insets show the far field images of emission pattern from a ZnS NW (left) and a ZnO nanodisk (right), respectively.

At present, the mechanism of the two-photon pumped self lasing in the compound nanostructures is investigated by studying the lasing modes and the stimulated emission lifetime and comparing them with those in the one-photon pumping scheme. Time-resolved PL characterization is performed to measure the PL lifetime for different excitation fluence and various dimensions of the nanowires/rods and nanodisks. Since the exciton lifetime in many semiconductors was found to differ remarkably from the lifetime of the radiative recombination arising from multiexciton scattering and/or electron-hole plasma, it is possible for us to identify the mechanisms behind the TPA-induced self-lasing. In our study, the Kerr shutter technique has been employed to measure the radiative decay of the ZnO nanodisks, which reveals an ultrashort lifetime of 3-4 ps, suggesting the presence of many-particle effect in the stimulated emission process.

Due to the low TPA coefficients in semiconductor compounds, improving the pumping efficiency in the two-photon excited nanolasers is crucial to their practical applications. We

propose herein to accomplish the TPA enhancement in the nanowires and nanodisks by designing strong optical-confinement at the TPA wavelength: In ZnO nanowires, self lasing at λ=390nm can be realized by two-photon pumping at λ=700nm. While the nanowires function primarily as waveguide resonators at the lasing wavelength λ=390nm, they can also trap the excitation photons at λ=700nm with the properly designed geometric dimensions. It has been reported that the optical field in a ZnO nanowire is subject to the tight modal confinement due to the strong index contrast for the nanowaveguide structure. The localized field in ZnO nanowires can therefore be intensified to enhance the TPA in the nanostructures due to the quartic field dependence of the TPA strength.
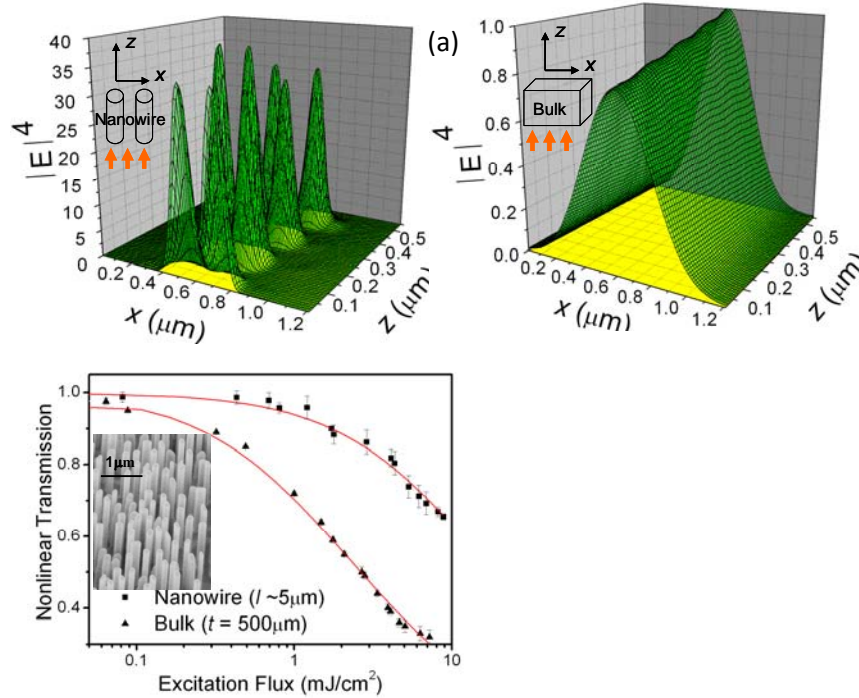

Figure 14: (a) top: Calculated E-field distribution ($|E|^4$) in sections of nanowire and bulk ZnO samples. (b) bottom: Nonlinear transmission curves of a ZnO nanowire film and a bulk ZnO crystal, respectively, at λ=700nm, with a peak excitation intensity of ~50 GW/cm^2. The inset shows the TEM image of the nanowire film sample.

In the study, the finite-difference time-domain (FDTD) calculation was performed to determine the electric field distribution, $|E(r,z)|^2$, in 180nm-diameter ZnO nanowires under λ=700nm light-illumination. The inter-wire distance was determined by assuming a 50% nanowire filling factor. Fig. 14(a) compares the computed field distribution in a linear array of four parallel ZnO nanowires and that in a bulk crystal. The fourth power of the field magnitude i.e., the quartic vale ($|E|^4$), was used in the comparison in view of the quartic field dependence of TPA. It is evident from the graph that the peak magnitude of the quartic electric field ($|E|^4$) in the ZnO nanowire is ~ 40 times higher than that in a bulk ZnO material. When the computed field distribution is spatially averaged for bulk and nanowire samples, respectively, the ratio is

reduced to ~12, suggesting that the TPA in ZnO nanowires can be enhanced by more than 10 times from the bulk case.

Experimentally we have conducted the nonlinear absorption measurement in ZnO nanowire samples of similar nanowire dimensions as in the computation. A large 'effective' TPA coefficient of $\beta_{effective}$=49.9cm/GW was obtained for ZnO nanowire arrays as compared to the bulk value of ~ 3.4 cm/GW, as shown in Fig 14(b) The ratio of the two TPA coefficients is ~14.7, which is in good agreement with the calculated enhancement factor.**Error! Bookmark not defined.** In this thrust we will design the dimensions of the nanowire waveguides based on the composition (ZnO, ZnS, GaN) as well as the excitation wavelength. The nanowires of pre-designed dimensions will be grown by the PI's collaborators at Georgia Tech (ZnO, ZnS) and Penn State (GaN), and will be tested at the PI's laboratory for the self-lasing actions in the TPA regime. It is expected that the local field-enhanced TPA in semiconductor nanowires can boost the two photon lasing efficiency and reduce the lasing threshold by an order of magnitude.

In NQD films the wave-guiding effect greatly modifies the angular distribution of the emission, making the output pattern highly dependent on film compositions and structures. Therefore, an efficiency characterization of NQD film emission cannot be accomplished by simply comparing the light output intensity with that of a reference dye sample as in the fluorescence-quantum yield measurements of NQD solutions, because this technique assumes an isotropic angular distribution of the fluorescent emission. A more suitable approach to characterize the emission efficiency of NQD films involves measurements using an integrating sphere. When a NQD film is placed inside an integrating sphere, the output emission of the film will be diffusely reflected by the barium sulfate coated inner surface of the sphere, and redistributed isotropically into the full range of solid angles. In this manner, the spectral and intensity detection of the light exiting from a small aperture in the sphere surface can be used for an accurate determination of the total number of photons emitted by the NQD film. The external differential quantum efficiency of NQD films, η, can then be calculated by its definition:

$$\eta_d = \frac{\text{number of photons emitted outward}}{\text{number of photons absorbed from the excitation source}}$$

We have conducted integrating sphere characterization of the external differential quantum efficiency of CdSe/CdS/ZnS core-shell NQD films. Efficiencies for both spontaneous and stimulated emission were studied over a wide range of optically excited NQD carrier densities, with the average number of photoexcited electron-hole pairs per nanocrystal achieved experimentally notated by $\langle N_{eh} \rangle$. A rapid rise in efficiency has been observed upon the transition from spontaneous to stimulated emission in our NQD films, with a maximum value of ~34% achieved with $\langle N_{eh} \rangle$~2.70. The emission efficiency declined gradually upon further increasing the

NQD excitation density. The competition between radiative exciton/bi-exciton recombination and the carrier density-dependent nonradiative recombination in NQDs was modeled to account for the observed variation of the external differential quantum efficiency. The model took into account the Poisson distribution of the photoexcited carriers as well as the unique, step-by-step Auger relaxation of the multiple electron-hole pairs in a quantum confined system. The lifetimes of the radiative bi-exciton recombination and the Auger relaxation in NQDs were also determined by comparing the model with the measured decay of the stimulated emission. The resulting Auger lifetime agrees well with the reported values that were previously extracted using time-resolved absorption spectroscopy, while the lifetime of the fast bi-exciton recombination in NQDs is determined for the first time, to the best of our knowledge.

5. Development of silicon-substrate-based PbSe quantum dot infrared light emitting diode

We have designed and characterized single-active-layer-structured infrared LED based on inorganic PbSe NQD and conjugated polymer MEHPPV. This is the first silicon-substrate-based infrared QD-LED reported. The device shows a strong infrared emission of ~1.55μm with an EQE of 0.3% which is highly desired for future high-speed circuit and system applications. An efficient Förster resonant energy transfer between the two components is determined as the dominant infrared emission mechanism. Promising ways to obtain stronger infrared emission includes reducing the trap density and improving energy transfer efficiency between the organic/inorganic components. Other investigations attempting to narrow the emission width is currently underway to bring it closer to practical application.

In the present work, PbSe nanocrystal quantum dots (NQDs) are synthesized by the noncoordinating solvent technique [14] and the size of the nanocrystals is tunable by varying the growth time. Quantum dots with a size of 6nm in diameter correspond to a photoluminescence peak at ~1.55μm. To make the electrical contact and anode an ITO layer of 200nm is deposited on silicon by RF sputtering process. A single active-layer structure is used in the device. The QD is mixed with the polymer to make the solution from which the single active layer is made. The device structure can be shown as ITO/ Poly(3,4-ethylenedioxythiophene) poly(styrenesulfonate)(*PEDOT:PSS*)/poly[2-methoxy-5-(2'-ethyl-hexyloxy)-1,4-phenylene vinylene] (*MEH-PPV*) +QD/ aluminum tris(8-hydroxyquinoline) (*Alq₃*)/Ca/Al, in which PEDOT and the single active layer are spin casted on ITO respectively followed by baking processes. The electron transport layer Alq_3 and the Ca/Al cathode are added by thermal deposition. Figure 1 shows the device structure and energy band alignment. MEHPPV has a highest occupied molecular orbital (HOMO) level of 5.1eV which is very close to the work function of ITO/PEDOT to enhance hole transport. More importantly its band alignment with the PbSe QD is favorable for energy transfer between the two components. Alq3 is chosen as the electron transport layer (ETL) due to its good electron-transport capability and its interfacial phase

compatibility with the active layer. All the measurements were performed with the device operating in air at room temperature. The luminescence is collected by an optical fiber and detected by a silicon/InAs thermoelectric cooled 2-color photodiode coupled with a monochromator. The *I-V* curve is collected by a Keithley 4200 semiconductor system while time-resolved PL traces are recorded with the Kerr shutter technique.
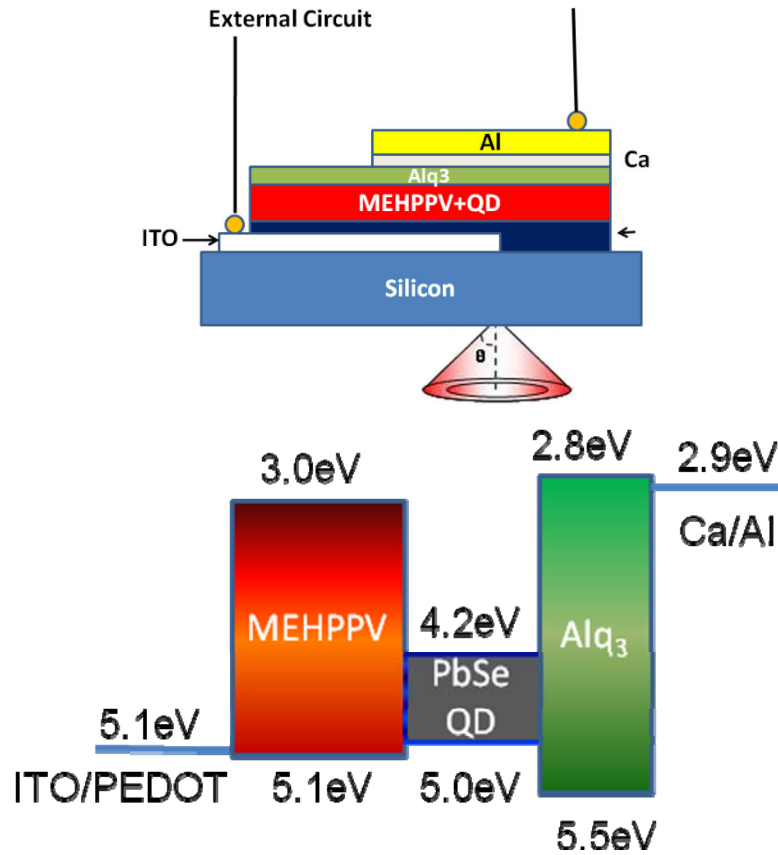

Figure 15. Device configuration and energy band diagram of a NQD-LED employing PbSe nanocrystals as the light emitting medium.

In the device the excitons can be generated in QD by direct charge injection or be transferred from polymer matrix by energy transfer. A multiple-layer-structured device was also fabricated but no EL was detected from the device. This indicates the direct charge injection mechanism is not effective. For an effective Förster resonance energy transfer (FRET) two prerequisites need to be satisfied: a short center-to-center separation distance between the two composites and a nonzero integral of the spectral overlap between donor emission and acceptor absorption[15, 16, 17, 18, 19]. MEHPPV is an efficient light emitting polymer with the dominant emission peak at ~600nm which overlaps with the QD absorption range. Additionally the MEHPPV serves as an

excellent polymer matrix to uniformly disperse QD and makes interacting molecules close enough to transfer energy (distance of FRET ~ 100A). Finally a uniform film is essential for making good electrode contact. The QD/polymer loading is also important for device performance since it helps to obtain an optimized balance between maximum infrared emission (from QD) and effective exciton production (from MEHPPV). A QD weight percentage of 30% is determined to be the optimized ratio for infrared light emission.

Under the forward bias condition, the LED emission covers a broad band between 1.4-1.65μm, as shown in the electroluminescence spectrum of the device . The electroluminescence is smooth and symmetric, showing a perfect fit to a Gaussian distribution. The L-I-V behavior of the device under forward bias is shown in Figure 16(a). The tested device exhibits a strong emission of ~26 μW under a current of 10mA and a voltage of 9.7V. This corresponds to an external quantum efficiency of ~0.3% which is much higher than the previous reported PbSe NQD based infrared LED and indicates an efficient infrared emission. The current-voltage measurement can also provide us information of current conduction mechanism. Figure 16(b) shows I-V characteristic for the infrared LED. At high voltage an $I \sim V^{m+1}$ relation is observed. From m we can determine the trap energy by the equation of

$$m = \frac{T_t}{T} = \frac{E_t}{kT}$$

where T_t is the characteristic trap temperature, E_t the characteristic trap energy, k the Boltzmann constant. By calculation the device shows high values of m at current up to 50mA (m=5.6). This indicates the presence of deep traps in the device which are not completely filled under high voltage. Therefore a promising way to improve device performance is to reduce the trap density significantly so that the light emission could happen under much lower voltage[20].

As mentioned above, the effective infrared emission is likely to be dominant by the Förster resonance energy transfer. To prove this, a profound knowledge of the underlying energy transfer processes is necessary. Upon optical pumping, the created excitons may decay to the donor polymer MEHPPV by radiative recombination (photoluminescence), nonradiative processes, or be transferred to QD nearby when they are sufficiently close. Excitons transferred from polymer to QD will also undergo radiative (lead to infrared light emission) and nonradiative processes. By measuring a QD/MEHPPV device emission power at visible and infrared region, we could obtain FRET efficiency as below,

$$E = \frac{\frac{P_{QD}}{\eta_{QD}} * \frac{2.0}{0.8}}{\frac{P_{MEHPPV}}{\eta_{MEHPPV}} + \frac{P_{QD}}{\eta_{QD}} * \frac{2.0}{0.8}}$$

In which P_{MEHPPV} and P_{QD} are the emission power of the device by MEHPPV (at 600nm) and QD (at 1500nm) respectively. The quantum efficiency of MEHPPV is denoted as η_{MEHPPV}, and similarly the quantum efficiency of QD is denoted as η_{QD}. The ratio of emitting photon energy difference between the two components is 2.0/0.8. For this experiment, a ratio of 7:5 of MEHPPV and QD emission has been obtained. By taking a η_{MEHPPV} of 13%[21] and a η_{QD} of 10% we have obtained a ratio efficiency of 70%. FRET efficiency can also be calculated from time resolved PL spectroscopy with the expression[18, 19]

$$E = 1 - \frac{\tau_{DA}}{\tau_D}$$

Where τ_{DA} is the fluorescence lifetime of the donor MEHPPV in the presence of the acceptor QD and τ_D is the fluorescence lifetime of the donor MEHPPV alone. Figure 17 shows the lifetime of the two solutions with the value of 147ps and 341ps which provides a FRET efficiency of 57%. The high FRET efficiency is very impressive compared to the MEHPPV PL efficiency. Considering most of the excitons provided in MEHPPV are wasted by non-radiative recombination an effective FRET process leading towards light emission at a longer wavelength will therefore provide an better way towards energy saving.
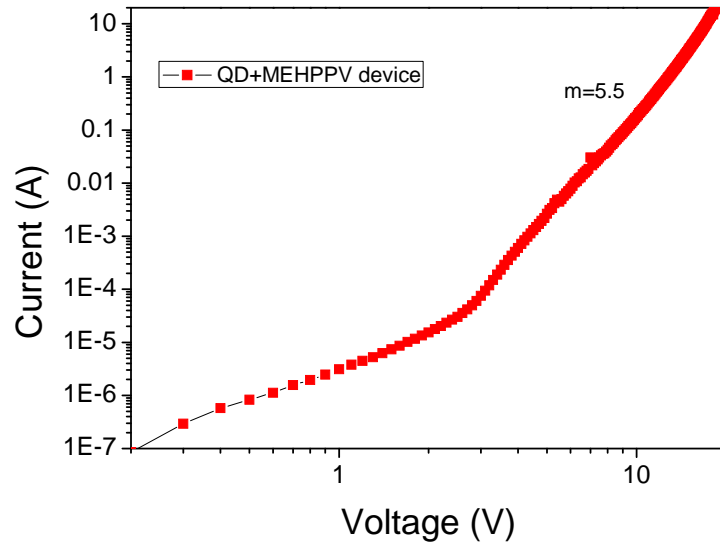

Figure 16(a). L-I-V characteristic of a typical silicon base MEHPPV/QD LED. The device structure is Si/ITO/PEDOT/MEHPPV+QD(60nm)/Alq3(30nm)/Ca(10nm)/Al(180nm). Inset: Current dependence of the device external quantum efficiency. (b). I-V characteristic in logarithmic scale of the device at forward bias.
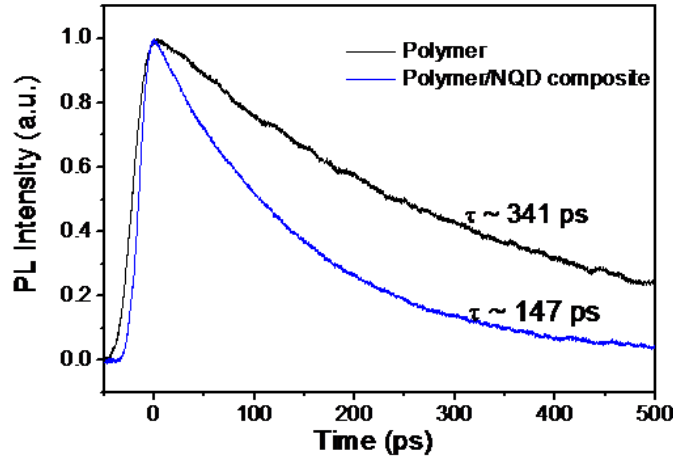
Figure 17. Time-resolved PL traces of MEHPPV in MEHPPV/QD mixture and pure MEHPPV solution. Femtosecond pulses at 510 nm (80 fs temporal duration, 1 kHz working frequency) from an optical parameter amplifier (TOPAS-C, Coherent) pumped by a Ti:Sapphire regenerative amplifier stage (Libra, Coherent) are employed to excite the PL from MEH-PPV. A 5-mm thick CS2 filled focused silica cell is chosen as the optical gate with temporal resolution of ~ 1.5 ps.

Besides the Förster resonance energy transfer, a traditional absorption-re-emission process is also potentially present for energy transfer. This process is not energy effective since several intermediate steps are involved, but it also needs to be considered as a potential infrared emission mechanism. For this calculation P_{MEHPPV}, P_{QD} and η_{QD} in the previous calculation are utilized. P_{MEHPPV}^0 is the assumed original power emitted by MEHPPV without the absorption of QD, it can be extracted from the absorption of QD at 600nm in the QD/MEHPPV film. After then the difference between the P_{MEHPPV}^0 and P_{MEHPPV} determines the largest possible energy absorbed by QD from MEHPPV. The upper limit of the infrared light emission from the absorption-re-emission process is estimated as,

$$P_{MEHPPV} = P_{MEHPPV}^0 \left(1 - A_{QD}^{@600nm}\right)$$

$$P_{QD}^{abs-re-emission} = \left(P_{MEHPPV}^0 - P_{MEHPPV}\right) * \eta_{QD} * \frac{0.8}{2.0}$$

In which $P_{QD}^{abs-re-emission}$ is the largest infrared power emitted from QD by the absorption-re-emission process, $A_{QD}^{@600nm}$ indicates the QD absorption in the real MEHPPV/QD thin film at 600nm, $A_{QD}^{@600nm}$ is taken as 0.0273. The extraction efficiency of visible and infrared light in the device is very close, so that the original visible and infrared light has the same intensity ratio as

the extracted light. The calculated $P_{QD}^{abs-re-emission}$ accounts for only 0.35% of the infrared emission P_{QD} which means the absorption-re-emission process could not explain the strong infrared emission. This provides more strong evidence that the main fraction of the NQD emission in our structure is activated by non-radiative energy transfer from the MEHPPV composite.

6. Monte Carlo study of PbSe quantum dots as the fluorescent material in luminescent solar concentrators

Luminescent solar concentrators (LSCs) redirect light to the edges of a planar waveguide via the total-internal-reflection (TIR) of photons emitted by fluorescent materials. Photovoltaic (PV) cells coupled to the edges of LSCs are used to convert fluorescence emission to usable electricity. Fluorescence light concentration reduces solar power conversion costs by reducing the required area of expensive PV cells. Additionally, LSCs eliminate the need for expensive solar tracking devices due to efficient absorption of diffuse light . Fluorescent materials used in LSCs had previously been limited to organic dyes. Recently, the development of new inorganic materials such as semi-conducting quantum dots (QDs) sparked research interests due to their large absorption spectra and tunable absorption/emission characteristics. Quantum dots benefit from their broad absorption spectrum and relatively narrow emission spectrum, tunable absorption/emission characteristics. PbSe QD LSCs are modeled using an LSC Monte Carlo ray-tracing simulation. We developed the LSC Monte Carlo simulation to determine the absorption efficiency, optical efficiency, power conversion efficiency, flux gain, and contribution of each individual loss mechanism in the LSC system. Our work suggest that Tandem LSC configurations, which utilize stacks of LSCs with different fluorescent materials to maximize power conversion efficiency, may benefit from the addition of a PbSe QD LSC layer to harvest infrared photons.

The LSC Monte Carlo simulation was created using GoldSim Pro Academic Version to evaluate the performance of PbSe QD LSCs. Absorption spectra, emission spectra, and quantum yield were used to simulate the optical properties of PbSe QDs. The percent absorption vs. wavelength spectra for any PbSe QD solution concentration and LSC thickness can be modeled using the Beer-Lambert law. To begin the simulation, a photon wavelength is generated by the AM 1.5G solar spectrum obtained from NREL. The probability of reflection at the front surface of the LSC waveguide is determined by calculating the Fresnel reflection coefficient of the incident photon at the air-waveguide interface. The probability of absorption is then determined by comparing the wavelength of the generated photon to the percent absorption vs. wavelength spectrum for a given solution concentration and LSC thickness.

Our simulation suggests that PbSe QDs with quantum yield of 0.80 function relatively well as the fluorescent material for LSCs at the specified dimensions, albeit with low power conversion efficiency below 1.0% if a BSR isn't used. For all the simulated LSCs with optimized concentrations and quantum yield of 0.80, flux gain is greater than 1. Therefore, these LSCs are functioning effectively as solar concentrators. Furthermore, simulation results show that the addition of a BSR to a PbSe QD LSC can boost power conversion efficiency above 1.0% while simultaneously improving flux gain. The addition of a BSR is particularly effective in PbSe QD LSCs due to the high incidence of self absorption. Since the addition of a BSR effectively doubles the solar absorption path length, self-absorption can be reduced while maintaining absorption characteristics by reducing the fluorescent material concentration.

In the present wrokm PbSe QD LSCs will also be used in tandem concentrator configurations to improve LSC efficiencies by collecting infrared photons that cannot be harvested by conventional, visible-emitting LSCs. Table 1 shows results from several Red305/PbSeQD tandem LSC simulations.

TABLE 1. LSC Monte Carlo simulation results for a baseline Red305 LSC and Red305/PbSeQD tandem LSCs with A_{LSC}=300×300 mm^2.

Fluor. Mater.	t (mm)	G	BSR	η_{QY}	c (μM)	η_{opt} (%)	η_{PCE} (%)	F_{PCE}
Red 305	2.5	30	No	0.98	300	8.56	4.86	6.27
Red 305	2.5	30	Yes	0.98	300	10.1	5.75	7.43
Red 305	2.5	30	No	0.98	300	8.58	4.89	6.31
PbSeQD	2.5	30		0.80	3.46	5.63	0.36	2.00
Red 305	2.5	30	Yes	0.98	300	8.75	4.98	6.44
PbSeQD	2.5	30		0.80	7.47	7.14	0.43	2.39

Tandem LSCs were simulated using Lumogen F Red305 dye in the top LSC coupled to high-efficiency GaAs PV cells, and PbSe QDs with η_{QY} of 0.8 in the bottom LSC coupled to Ge TPV cells. For LSCs to act in tandem electrically as well as optically, the solar cells between the two LSCs will either need to be connected in parallel or series, resulting in losses if voltage or current are not matched respectively. Simulation results suggest that PbSe QD LSCs are capable of improving the η_{PCE} of a Red305 LSC system by nearly 10%.

7. Near-Band-Edge Electroluminescence from Heavy Metal-Free Colloidal Quantum Dots

We demonstrate near-band-edge electroluminescence emission from the heavy-metal-free colloidal quantum dots (QDs) consisting of CuInS$_2$-ZnS alloyed (ZCIS) cores and ZnSe/ZnS double shells. The QDs were synthesized with a high-temperature organic solvent method and exhibit size-tunable absorbance and photoluminescence. The composition of the alloyed ZCIS cores was determined with inductively coupled plasma atomic emission spectrometry and

energy-dispersive x-ray spectroscopy. Bright and organic-free electroluminescence emission peaked at red (λ=623nm), yellow (λ=594nm), and green (λ=560nm) wavelengths was observed from the heavy metal-free QD-LEDs comprising, respectively, ZCIS/ZnSe/ZnS core-shell QDs of 2.3nm, 2.7nm, and 3.3nm-diameters. The brightness, onset voltages, luminance output uniformity, and efficiencies of QD-LEDs were characterized. Finally, carrier recombination in the ZCIS/ZnSe/ZnS core-shell QDs was investigated with time-resolved photoluminescence, revealing a sub-microsecond luminescence lifetime. The fast relaxation, in conjunction with the pronounced size-dependence of the QD luminescence wavelength, confirms the near-band-edge nature of the optical transitions in the nanoparticles.

A serious drawback of the present colloidal QD-LED technology is its dependence on heavy-metal cations, such as cadmium, lead, and mercury. These heavy-metal compositions are regarded as 'purely toxic'[22] and raise concerns about disposal, carcinogenity, and other health risks. The regulatory acceptance of these nanocrystal materials containing heavy-metal constituents could severely hinder the ultimate research transformation and commercialization of the QD-LED technology. Toward this end, intensive research studies have been conducted to develop colloidal QD-LEDs free of cadmium, lead, and mercury compositions. While a broad range of compound and elemental semiconductors, including (Ga,In)(N, P), Zn(O, S, Se), Si, and Ge, have been exploited to design and synthesize colloidal quantum dots that are more environmental-friendly and nontoxic, there have been very limited successes in obtaining EL emission from these solution-processed nanocrystals, let alone their application in LEDs. To date, only deep-level or surface-state associated EL was observed from Mn-doped ZnSe/ZnS colloidal quantum dots and silicon nanocrystals.[23,24] The broadly-distributed energy states and prolonged relaxation processes that are characteristic of the deep recombination centers in the mid-bandgap, however, give rise to fundamental limitations to the luminescence spectral control, quantum yield and effectiveness of carrier injection in those semiconductor nanoparticles, leading to size-independent, broadband EL emission of extremely-low efficiencies as well as the high-voltage, alternating bias ($\geq$100 V peak-to-peak) for device operation.

The core-shell QDs employed in our heavy-metal-free LED devices have $CuInS_2$-ZnS alloyed cores and ZnSe/ZnS double shells, and were synthesized with an approach modified from that originally proposed by Maeda *et al.*[25] The tri-*n*-octylphosphine/oleylamine/octadecene mixture was used to provide the solvent environment for the nucleation and growth of $CuInS_2$-ZnS alloyed cores from zinc diethyldithiocarbamate (DECZn), CuI, and InI_3 precursors at elevated temperatures (150-180 ºC). For nanocrystal nucleation, DECZn decomposes to ZnS as the temperature rises beyond 150°C, while the excess sulfur reacts with copper and indium iodide to form the alloyed nuclei. During the subsequent crystal growth, the ultimate size of the nanoparticles was controlled by varying the reaction temperature and time. In bulk $CuInS_2$-ZnS alloyed crystals, zinc atoms have been found to preferentially substitute for copper atoms due to their similar size. The introduction of Zn ions into $CuInS_2$ lattices is therefore energetically favorable because it reduces the population of anti-site defects due to Cu vacancies in the nano-

crystalline lattice, which, in turn, is expected to improve the PL efficiency of the alloyed nanocrystals. Following the growth of ZCIS cores, a monolayer of ZnSe shell was epitaxially grown over their surfaces using the SILAR method. This involves dropwise and alternate addition of the solutions of zinc and selenium precursors (ZnO/oleic acid/octadecene and Se/tri-n-butylphoshine) at 200 °C and annealing the nanocrystals at 150 °C for 2 hours. Next, the nanoparticles were overcoated with the second ZnS shell by adding into the reaction solution a predetermined amount of DECZn in ODE (16.7mM) at 200 °C. The growth of ZnS shells continued for 10 min, and was completed with annealing at 150 °C for 2 hours. Finally, 1-dodecanethiol (CH3(CH2)11-SH) was added into the solution of the QD product because the dodecanethiol coordinates strongly to the metal cations on nanocrystal surfaces and functions as a ligand.

In the present study, red-, yellow- and green-emitting ZCIS/CdSe/CdS core-shell QDs have been synthesized with the above-mentioned approach, as shown in Fig. 1(f). For their use in QD-LEDs, the purified core-shell QDs were subjected to a multi-step precipitation/redissolvation process of purification and subsequently dried into solid powders. Some of the nanocrystals were re-dispersed in toluene and tetrachloroethylene for microscopic and spectroscopic analyses, respectively.

Transmission electron microscopy (TEM) of the purified QDs was performed on a JEOL EM-2010F microscope operating at 200 keV. The QD cores prepared without shells had an average diameter of 2.7 nm. In the diffraction pattern collected from many QDs , the ring pattern reveals interplanar spacings of 0.314 nm, 0.193 nm, and 0.166 nm. For chalcopyrite $CuInS_2$ with lattice parameters of $a = 0.5523$ nm and $c = 1.1133$, the five most intense reflections expected in a diffraction pattern are for interplanar spacings of 0.320 nm, 0.196 nm, 0.195 nm, 0.168 nm, and 0.167 nm. In addition, we note that the lattice parameters of $CuInS_2$ would be reduced due to incorporation of ZnS. Therefore, the chalcopyrite structure matches the diffraction pattern from the QDs fairly well within experimental error (within 2%). With the ZnSe/ZnS double shells added, the QDs are approximately 3.3 nm in diameter, suggesting a monolayer shell thickness (0.3nm/ZnSe monolayer). There is no obvious disruption of the crystal structure due to the addition of the very thin shell. The diffraction pattern collected from many QDs is very similar to that from the cores. In this case, the interplanar spacings are measured to be 0.322 nm, 0.195 nm, and 0.168 nm, which is again consistent with chalcopyrite $CuInS_2$-ZnS. Apart from the red QDs, the diameters of yellow- and green-emitting ZCIS/ZnSe/ZnS core-shell nanocrystals were also measured by TEM to be ~2.7nm and ~2.3nm, respectively.

The molar ratio of $CuInS_2$ to ZnS compositions in the alloyed ZCIS nanocrystal cores was determined with inductively coupled plasma atomic emission spectrometry (ICP-AES) using a standard digestion method. The measured elemental ratio of Zn: In: Cu: S is ~ 2.7: 1.0: 1.0: 6.4, suggesting that the alloyed nanocrystals contain ~43% $Cu_{0.5}In_{0.5}S$ and ~57% ZnS on a molar basis, or ~48% $CuInS_2$ (or $Cu_{0.5}In_{0.5}S$) and ~52% ZnS by weight. In the elemental ratio sulfur in excess of the stoichiometric value (~4.7) is due to the presence of the sulfur-containing

dodecanethiol ligand in the solution of ICP samples. The alloy composition was further confirmed with energy-dispersive x-ray spectroscopy (EDX), as shown in Fig. 2, which reveals the elemental ratio of Zn: In: S = 3.0±0.3 : 1.0 : 5.0±0.5 for the ZCIS cores of the red-emitting QDs in the present study. Quantification was performed by using the ES Vision software package with theoretically calculated k-factors. It is noted that the copper peaks in the EDX spectrum largely arise from the copper grid that was used to hold the QD sample in the TEM measurement and therefore can not be used to determine the copper contents in the nanocrystals.

The absorption and PL spectra of red, yellow and green core-shell QDs dispersed in tetrachloroethylene were measured, which exhibit, respectively, absorption cut-offs at 501nm, 471nm, and 445nm, and PL maxima at 620nm, 580nm and 553nm for red, yellow and green nanocrystals. The full-width-at-half-maximum (FWHM) bandwidths of the luminescence emission are between 90nm–95nm, while the PL quantum yields were determined to be ~60%, ~40%, and ~45% for red, yellow and green QDs, respectively, by comparing the integrated fluorescence intensities with that of standard dye solutions. While the lack of well-defined exciton peaks in the QD absorption and the broadband PL emission are reminiscent of the controversial nature of donator-acceptor pair (DAP) transitions reported in some I-III-VI nanocrystals, our TRPL characterization reveals a fast carrier recombination of hundreds of nanoseconds in lifetime: The second harmonic (λ=400 nm) of the output of a Ti:sapphire femtosecond amplifier (1 kHz, 80fs, Coherent Libra system) was used to photoexcite the QD samples, and the PL lifetimes for red, yellow and green ZCIS QDs were measured with a fast photomultiplier (Hamamatsu R28) to be 315ns, 300ns, and 265ns, respectively. This is in sharp contrast to the prolonged PL lifetime (up to 250μs) that is associated with the deep-energy center emission in Mn- or Cu-doped ZnS nanocrystals. It is therefore possible to achieve high-efficiency EL emission with the ZCIS/ZnSe/ZnS core-shell QDs exploited in the present study. Nose *et al.* have recently identified a similar, nanosecond-timescale relaxation characteristic in ZCIS nanocrystals, and assigned the fast radiative recombination to a near-band-edge transition that involves the quantum confined conduction band and a V_{cu} acceptor level.[26]

Apart from the TRPL study, the insight to the emission mechanism of ZCIS QDs can also be gained from the observation that there is a pronounced spectral shift (~67nm or 340 meV) for PL emission as the size of the ZCIS cores of the QDs is reduced from 3.3nm to 2.4nm, which is too large for DAP recombination or for any radiative transition between a pair of deep levels. The size-induced PL shift for a DAP recombination comes only from the change in the Coulomb interaction with changing DAP separation, *r*, according to the equation[27]

$$E_{DAP} = E_g - E_D - E_A + \frac{e^2}{4\pi\varepsilon r} \qquad (1)$$

where E_{DAP} and E_g are the DAP recombination energy and bulk energy band gap, respectively; E_D and E_A are the respective ionization energies of the donor and acceptor levels; and ε the electric permittivity. Using Eq. 1, the energy shift associated with Coulomb interaction was

calculated to be only ~20.3 meV when the ZCIS QD size is reduced from 3.3nm to 2.4nm in the present work.

The heavy-metal-free nature and the promising luminescence properties of the ZCIS/ZeSe/ZnS core-shell QDs have prompted us to exploit their applications in QD-LEDs. A multilayer LED structure has been employed in device fabrication, which consists of, from the bottom up, a glass substrate, a layer of poly(3,4-ethylene dioxythiophene) doped with poly(styrenesulfonate) (PEDOT:PSS), a poly(N,N'-bis(4-butylphenyl)-N,N'-bis(phenyl)benzidine) (poly-TPD) hole-transport layer (HTL), an emissive region of ZCIS/ZeSe/ZnS core-shell QDs, a tris-(8-hydroxyquinoline) aluminum (Alq3) electron-transport layer (ETL) (in the red QD-LED), and a Ca/Al bi-layer top electrode. The nominal thicknesses of the pre-coated ITO layers on glass is ~200nm, with the respective sheet resistance measured to be ~20 Ω/square.

The output spectra of the QD-LEDs are presented in Fig. 18. The output of the red, yellow, and green devices exhibits peak wavelengths at 622nm, 591nm, and 560nm, respectively. The emission peaks of all three LEDs are red-shifted by 2-10nm in wavelength from the PL maxima measured in the solution due to the Föster energy transfer in close-packed QD solids. The FWHM EL bandwidth of red, green and yellow QDs was measured to be 106nm, 125nm, and 102nm, receptively, exhibiting some broadening from the corresponding PL profiles. Unlike the EL spectra of Mn-doped ZnS nanocrystals, there was no noticeable side-band deep-trap emission from the ZCIS/ZnSe/ZnS QD-LEDs in the present study. The photographs in the insets of Fig. 3 display, respectively, the close-up view of the surface emission from the red, yellow, and green QD-LEDs operated at a brightness of ~100 cd/cm^2. The images reveal the spectral and luminous uniformity across the device emissive regions. The organic emission in the red QD-LED output has been minimized via controlling the HTL and ETL layer thicknesses in the device.
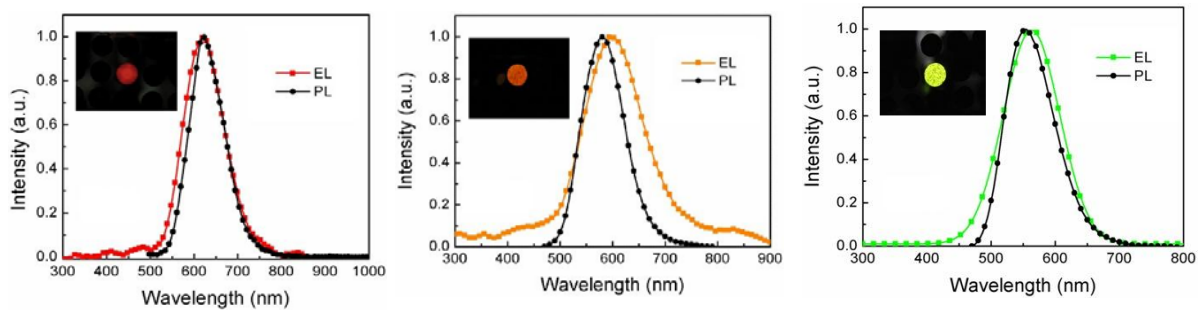

Figure 18: The output spectra of the (a) red, (b) yellow, and (c) green QD-LEDs. The photographic images in the insets of (a)-(c) display, respectively, the close-up view of the surface emission of the respective QD-LEDs operated at a brightness of ~100 cd/cm^2.

8. Efficient emission from direct bandgap transitions in n-doped germanium under ultrashort pulse excitation.

Direct bandgap-associated emission in Ge is peaked at the wavelength of ~1550 nm (0.8 eV), which is coincident with the most technically-important wavelength for optical communication. To improve the efficiency of emission from the direct bandgap transitions, strategies have been employed to compensate for the energy difference between the valleys of indirect and direct gaps, such as the n+ doping design and tensile strain engineering. In this study, we developed a method of compensating for the energy difference between the valleys of indirect and direct gaps with high density carriers photogenerated by ultrashort light pulses. Efficient Ge emission arising from direct band transitions was observed with the intense pulse excitation; and amplified spontaneous emission (ASE)-like emission was observed from heavily n-doped Ge samples.
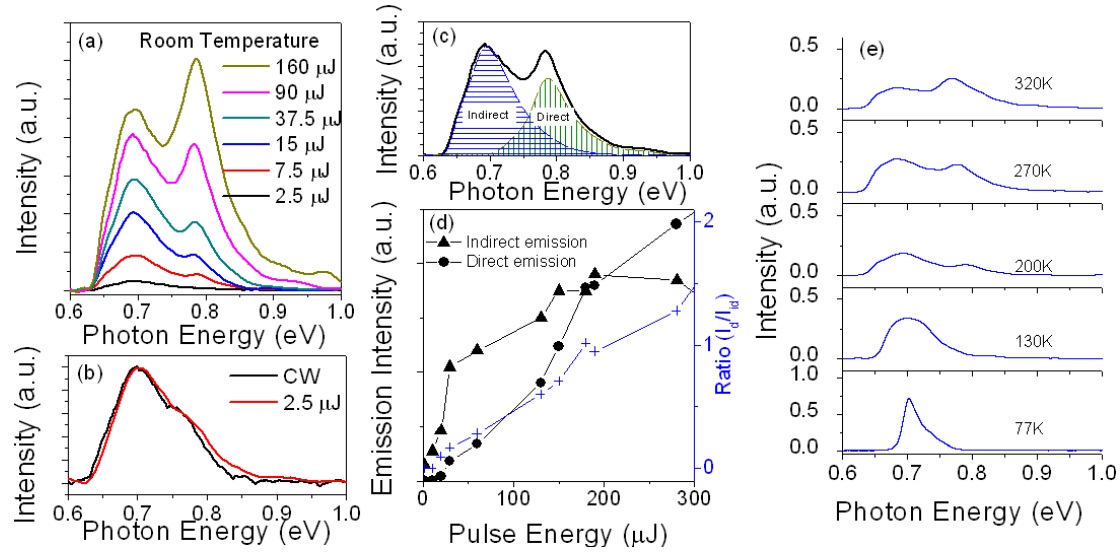

Figure 19. (a) Room temperature emission spectra from Ge film with different excitation pulse energy. (b) a comparison of the emission spectra under cw excitation and weak pulse excitation. (c) Fitting of emission from indirect emission band and direct emission band. (d) Excitation pulse energy dependence of the indirect emission and direct emission: the ratio shows increase of efficiency from direct band gap with the excitation pulse energy. (e) Emission spectra recorded at different temperature.

The nanoparticle samples used in this study were grown on Ge substrate with APCVD system and the n-doping was introduced with P-doping. Femtosecond pulses from a regenerative amplifier system (80 fs, 1 kHz, Libra, Coherent) with variable pulse energy were used to pump the Ge samples in the experiment. Time-integrated emission spectra were recorded with a liquid nitrogen cooled InGaAs detector with an extended response wavelength range (800 nm ~ 2200 nm), and time-resolved PL traces at 1550 nm were recorded by a fast photomultiplier tube (PMT) (H 10330A-75, Hamamatsu) with the nanosecond-resolution. Double side polished Si wafers were employed to prevent the excitation residual from reaching the PMT during the measurement.

With low pulse energy excitation, the PL spectrum of the Ge sample is similar to the emission at cw excitation (Fig.19), and the indirect emission dominates. With increase of excitation pulse energy, emission from direct bandgap grows rapidly, and the ratio of intensity of direct emission to that of indirect emission increases accordingly, indicating that the high density carriers photo-generated by the intense pulses excitation can be used to fill the indirect valley. As more free carriers start to populate the direct valley, direct bandgap associated emission becomes more efficient. The postulation was examined by the temperature dependent study (Fig.19 e), where most of the carriers occupy in the low levels at a low temperature.

Time-resolved PL traces show a decrease of the room-temperature lifetime of direct band emission from ~ 50 ns to ~ 30 ns, suggesting that the possibility of electron-hole plasma generation following the direct bandgap transition. Our calculation has suggested that such a high carrier density carriers will be sufficient to produce some optical gain. Furthermore, in order to reduce the threshold for a potential gain in Ge, experiments were carried out with the samples of different n-type doping concentrations. As shown in Fig. 20, the efficiency of direct emission increases with the n-doping concentration due to the pre-filling of indirect valley with the majority carriers provided by the dopant impurities. With those heavily-doped n+ Ge samples, enhanced emission with narrowing profile can be achieved under intense pulse excitation, which suggests the possibility of achieving stimulated emission in Ge.
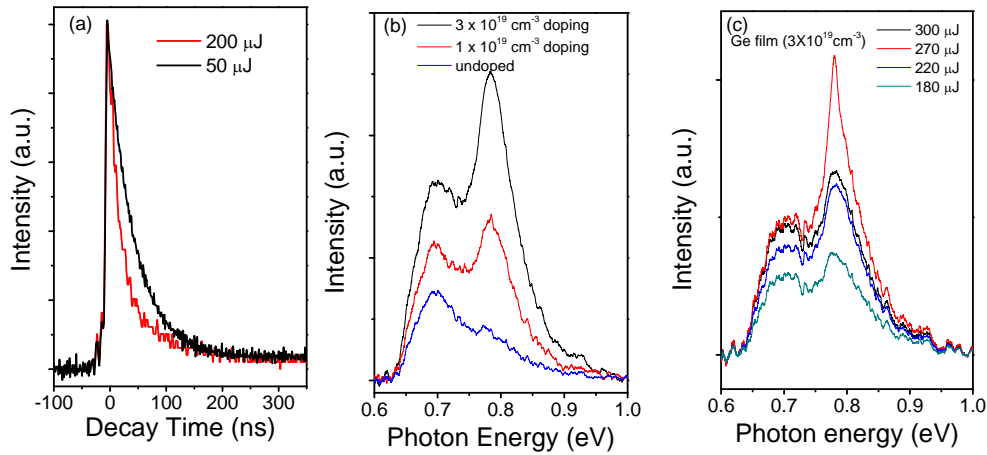

Figure 20. (a) Time-resolved traces of PL emission at 0.78 eV with low and high pulse energy excitation. (b) Emission spectra recorded from samples with different doping. (c) Emission spectra recorded from a Ge film with high N-doping with excitation power near the damage threshold.

Reference

[1] T.J. Prosa, M.J. Winokur, J. Moulton, P. Smith, A.J. Heeger, "X-ray Structural Studies of Poly(3-alkylthiophenes): An Example of an Inverse Comb", Macromolecules, **1992,** 25, 4364,

[2] Nozik, A.J. Physica E, **2002,** 14, 115

[3] Sargent, E. H. Adv. Mater., **2005,** 17, 515

[4] Halls, J. J. M.; Pichler, K.; Friend, R. H.; Moratti, S.C.; Holmes, A. B. Appl. Phys. Lett. **1996,** 68, 3120

[5] Jason, M. D.; Paul, B. F. J. Phys. Chem. B., **2002,** 106, 4632

[6] Wehrenberg, L. B.; Guyot-Sionnest, P. Journal of the American Chemical Society, **2003,** 125, 7806

[7] Jarosz, V. M.; Stott, E. N.; Drndic, M.; Morgan, Y. N.; Kastner, A. M.; Bawendi, G. M. Journal of Physical Chemistry B., **2003,** v107, n46, 12585

[8] Ginger, S. D.; Greenham, C. N. Journal of Applied Physics, **2000,** 87, 1361

[9] Bube, R. Photoelectronic properties of semiconductors, Cambridge University Press, 1st edition, **1992**

[10] Qasrawi A. F.; Gasanly, N. M. Semicond. Sci. Technol. **2005,** 20, 446

[11] Tabak M.; Warter, J. Jr. Physical Review, **1966,** 148, 982

[12] Bakueva, L.; Musikhin, S.; Hines, A, M.; Chang, F. T. -W.; Tzolov, M.; Scholes, D. G.; Sargent, H. E. Appl. Phys. Lett., **2003,** 82, 2895

[13] H. Du, C. Chen, R. Krishnan, T. D. Krauss, J. M. Harbold, F. W. Wise, M. G. Thomas, and J. Silcox, "Optical Properties of Colloidal PbSe Nanocrystals," **2002**, Nano Lett. **2**, 1321

[14] W. Yu, J.C. Falkner, B.S. Shih, V.L. Colvin, Chemistry of Materials, **2004,** 16, 3318

[15] T. Förster, Ann. Phys. **1948,** 6, 55

[16] G. Juzeliunas, and D.L. Andrews, Advanced Chemical Physics, **2000,** 112, 357

[17] M. Hopmeier, W. Guss, M. Deussen, E.O. Gobel, and R.F. Mahrt, Physical Review Letters, **1999,** 82, 4118

[18] J.R. Lakowicz, Principles of Fluorescence Spectroscopy, 2nd edition; Kluwer Academic: New York, **1999**

[19] A.R. Clapp, I.L. Medintz, J. M. Mauro, B.R. Fisher, M.G. Bawendi, H. Mattoussi, Journal of American Chemical Society, **2004,** 126, 301

[20] A. Carbone, B.K. Kotowska, D. Kotowski, Physical Review Letters, **2005,** 95, 236601

[21] J. Morgado, R. Iqbal, G. Yahioglu, L.R. Milgrom, S.C. Moratti, A.B. Holmes, R.H. Friend, F. Cacialli, Materials Research Society Symposium - Proceedings, **2000,** v 598, p BB3.57.1-BB3.57.8

[22] Heavy metals in the environment, Bibudhendra Sarkar, Published by CRC Press, **2002,**

ISBN 0824706307, 9780824706302

[23] J. De La Torrea;∗, A. Soui'a, A. Ponceta, C. Bussereta, M. Lemitia, G. Bremonda,G. Guillota, O. Gonzalezb, B. Garridob, J.R. Moranteb, C. Bonafosc, "Optical properties of silicon nanocrystal LEDs", Physica E 16 **2003,** 326 – 330

[24] Vanessa Wood,†,‡ Jonathan E. Halpert,†,§ Matthew J. Panzer,‡ Moungi G. Bawendi,§ and Vladimir Bulovic, "Alternating Current Driven Electroluminescence from ZnSe/ZnS:Mn/ZnS Nanocrystals", Nano Lett., online early posting,

[25] Masato Uehara,1,a Kosuke Watanabe,2 Yasuyuki Tajiri,2 Hiroyuki Nakamura,1 and

Hideaki Maeda1,2,3, " Synthesis of CuInS2 fluorescent nanocrystals and enhancement of fluorescence by controlling crystal defect ", J. Chem. Phys. **2008,** 129, 134709

[26] Katsuhiro Nose, Naoya Fujita, Takahisa Omata, Shinya Otsuka-Yao-Matsuo,

Wataru Kato, Masato Uehara, Hiroyuki Nakamura, Hideaki Maeda, Hayato

Kamioka4, and Hideo Hosono, Journal of Physics: Conference Series **2009,** 165, 012028

[27] Katsuhiro Nose, Takahisa Omata, and Shinya Otsuka-Yao-Matsuo, J. Phys. Chem. C **2009,** 113, 3455–3460